COURSE 4

ATOM INTERFEROMETRY

S. CHU

Physics Department, Stanford University, Stanford, CA 94306-4060, U.S.A.

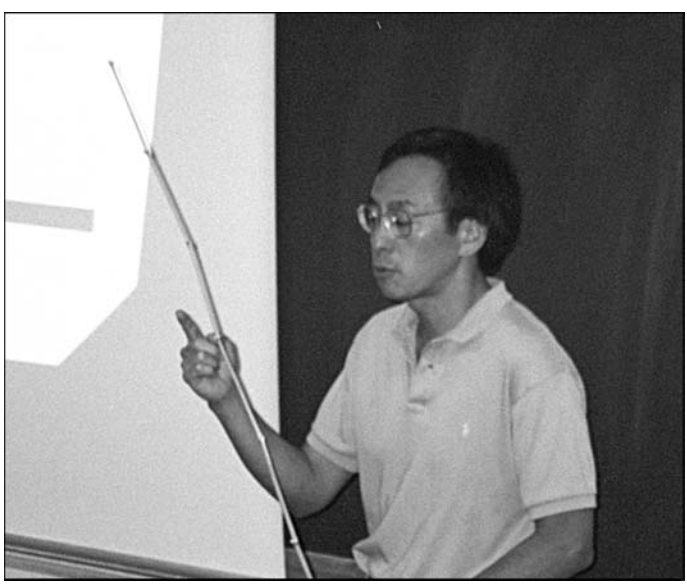

Contents

ATOM INTERFEROMETRY

S. Chu

1 Introduction

The first demonstrated atom interferometers, reported in 1991 by Carnal and Mlynek [1] and Keith *et al.* [2] were based on the diffraction of atoms with micro fabricated structures. This class of atom interferometers is analogous to optical interferometers, where slits or diffraction gratings have been used to divide and recombine beams of atoms. The gratings and slits can be either material structures or periodic light fields. Three months later, atom interferometers based on optical pulses of light were reported by Riehle *et al.* [3], and by Kasevich and Chu [4] In this class of interferometers, the spatial separation of the atoms is accomplished by the momentum recoil induced by the electromagnetic field used to drive the atoms from one internal state to another. Thus, the internal and external degrees of freedom are intimately connected.

Atom interferometry has attracted significant interest for a number of reasons. (i) Atoms possess internal degrees of freedom so that the interferometers that combine interference effects from both the internal and external degrees of freedom can be constructed. (ii) Their internal states are easily manipulated by external magnetic, electric or electromagnetic fields. (iii) Different atoms possess a wide range of different properties that offer the experimentalist an opportunity to address a wide range of problems. (iv) The technologies of laser cooling and atom trapping allow extraordinarily long quantum measurement times so that atom interferometers of great precision can be constructed.

In this set of lectures, we will first present a development of the fundamental principles of atom interferometers. Next, we will discuss a few of the various methods now available to split and recombine atomic de Broglie waves, with special emphasis on atom interferometers based on optical pulses. These interferometers are the intellectual grandchildren of magnetic resonance methods that were later generalized to electronically excited states of atoms. Consequently, the wealth of theoretical and experimental techniques that have been developed for over a half century can be exploited

for atom interferometry. We will also be particularly concerned with high precision interferometers with long measurement times such as those made with atomic fountains. Some applications and the systematic effects encountered in those applications will also be covered. Finally, the outlook of future developments will be given.

2 Basic principles

We will be concerned with single particle interference in which each atom interferes with itself and only itself. Virtually all photon and matter wave interferometers demonstrated to date are of this type. Our quantum states may be described in terms of a set of pure states defined as a tensor product of the Hilbert space describing the internal energy state of the atom and the Hilbert space describing the external degrees of freedom,

$$|\Psi\rangle = \sum_n |n\rangle \otimes |c_n\rangle \tag{2.1}$$

where $|n\rangle$ and $|c_n\rangle$ are internal state and external state parts of the atom. The external state can be described by the center of mass position and $|\Psi\rangle$ will have an associated wave function $\Psi(\mathbf{x}, t)$. Alternatively, the external state can be described by momentum plane waves. This approach will be developed in Section (2.5).

2.1 Ramsey interference

An early example of an atom interference is the Ramsey method of separated oscillatory fields [6]. In this type of interferometer, only the internal states $|n\rangle$ contribute to the interference. An atom in an atomic beam initially in the ground state is placed into a superposition of states $|e\rangle$ and $|g\rangle$ as it passes through a microwave cavity. The atom then travels over some distance into a second microwave cavity where the atom is placed into another superposition state that depends on the phase of the atom superposition state relative to the phase of electromagnetic field in the second microwave cavity. Finally, the interference is measured by projecting the atomic state onto one of the quantum states, say $|g\rangle$, of the system. Interference requires that it is impossible to distinguish which path the atom took. Thus, the two alternate paths $|g\rangle \to |e\rangle \to |g\rangle$ and $|g\rangle \to |g\rangle \to |g\rangle$ should not have a measurable quantity that will allow one to differentiate the two trajectories. Since the small momentum recoil of an rf photon does not cause the two parts of the atom to spatially separate, the external degrees of freedom of the atom such as position and momentum can be assumed to be decoupled from the internal degrees of freedom. Later,when we generalize the treatment to include the recoil of an optical photon, we will have to consider the external state variables.

The time evolution of any quantum state[1]

$$|\Psi(t)\rangle = a_e(t)|e\rangle + a_g(t)|g\rangle \Leftrightarrow \begin{bmatrix} a_e(t) \\ a_g(t) \end{bmatrix} \tag{2.2}$$

is given by the Schrödinger equation

$$i\hbar \frac{\mathrm{d}}{\mathrm{d}t}|\Psi(t)\rangle = \hat{H}|\Psi(t)\rangle \cdot \tag{2.3}$$

The Hamiltonian for a two-level atom coupled to an electromagnetic field, in the absence of spontaneous emission, is

$$\begin{aligned} \hat{H} &= \hbar\omega_e|e\rangle\langle e| + \hbar\omega_g|g\rangle\langle g| - \mathbf{d}\cdot\mathbf{E} \\ &= \begin{bmatrix} \hbar\omega_e & V_{eg} \\ V_{eg}^* & \hbar\omega_g \end{bmatrix} \end{aligned} \tag{2.4}$$

where the electromagnetic field operator is

$$\mathbf{E} = \mathbf{E}_0 \cos(\omega_\mathrm{L} t + \phi), \tag{2.5}$$

couples to the atom *via* an electric dipole coupling term $V = -\mathbf{d}\cdot\mathbf{E} = |e|\mathbf{r}\cdot\mathbf{E}$, where $\mathbf{r}$ is defined as the vector from the nucleus of the atom to the electron position. The eigenfrequencies ω_e and ω_g represent the *total* energy of the atom, both internal and external, but if the kinetic energy of the atom is decoupled from the internal states, one may take these frequencies as the internal state energies. The matrix element V_{eg} is defined to be

$$\begin{aligned} V_{eg} &= \langle e|V|g\rangle \\ &= \hbar\Omega_{eg}\left(\frac{\mathrm{e}^{i(\omega_\mathrm{L}t+\phi)} + \mathrm{e}^{-i(\omega_\mathrm{L}t+\phi)}}{2}\right), \end{aligned} \tag{2.6}$$

and the Rabi frequency is defined as

$$\Omega_{eg} \equiv -\frac{\langle e|\mathbf{d}\cdot\mathbf{E}_0|g\rangle}{\hbar} \cdot \tag{2.7}$$

For simplicity, we will assume that the amplitude of the electric field $\mathbf{E}_0$ is constant when the light is on.

It is often convenient to go to a new interaction basis where $c_e(t)$ and $c_g(t)$ are slowly varying functions

[1]The double arrow denotes the correspondence between the state vector description and a particular representation given by the two-spinor. Henceforth, we will use the two descriptions interchangeably.

$$|\Psi(t)\rangle = \begin{bmatrix} c_e(t)\mathrm{e}^{-i\omega_e(t)/2} \\ \\ c_g(t)\mathrm{e}^{-i\omega_g(t)/2} \end{bmatrix}. \tag{2.8}$$

We also make the "rotating wave approximation" where the near resonant terms $\mathrm{e}^{i(\omega_{eg}-\omega)t'}$ are taken to be much larger than the off resonant terms $\mathrm{e}^{i(\omega_{eg}+\omega)t'}$, with $\omega_{eg} \equiv \omega_e - \omega_g$ and $\delta \equiv \omega_{\mathrm{L}} - \omega_{eg}$.

The Hamiltonian in this transformed frame becomes [8]

$$\hat{H}_{\mathrm{R}} = \frac{\hbar}{2} \begin{bmatrix} 0 & \Omega_{eg}\mathrm{e}^{-i(\delta t+\phi)} \\ \\ \Omega^*_{eg}\mathrm{e}^{i(\delta t+\phi)} & 0 \end{bmatrix}. \tag{2.9}$$

For nonzero detunings, the weakly *time-dependent* Hamiltonian can be turned into a *time-independent* Hamiltonian by the transformation of variables $c_e(t) = d_e(t)\mathrm{e}^{-i\delta t/2}$ and $c_g(t) = d_g(t)\mathrm{e}^{i\delta t/2}$. Physically, this transformation describes the quantum states in terms of a frame rotating about the **z**-axis with frequency δ. (Similarly, the transformation from the Schrödinger picture to the interaction picture can be viewed as a transformation to a frame rotating at ω_{eg}.) This transformation is analogous to the magnetic resonance transformation to the rotating frame in which the oscillating magnetic field inducing a transition on a spin-$\frac{1}{2}$ system appears as a static torque [7].

The transformation of a ket $|\Psi\rangle$ to a ket $|\Psi\rangle_{\mathrm{R}}$ in a frame rotated through an angle $-\delta t$ about the $\hat{\mathbf{z}}$-axis is given by

$$D(\hat{\mathbf{z}}, -\delta t)|\Psi\rangle = |\Psi\rangle_{\mathrm{R}}, \tag{2.10}$$

where the rotation operator $D(\hat{\mathbf{z}}, -\delta t)$ has the representation

$$D(\hat{\mathbf{z}}, -\delta t) \Leftrightarrow \mathrm{e}^{i\sigma_z\delta t/2} = \begin{bmatrix} \mathrm{e}^{i\delta t/2} & 0 \\ 0 & \mathrm{e}^{-i\delta t/2} \end{bmatrix} \tag{2.11}$$

where σ_z is a Pauli spin matrix [84].

The description of Schrödinger's equation in the rotating frame is found by starting with

$$i\hbar\frac{\mathrm{d}}{\mathrm{d}t}\left(D^\dagger|\Psi\rangle_{\mathrm{R}}\right) = \hat{H}\left(D^\dagger|\Psi\rangle_{\mathrm{R}}\right). \tag{2.12}$$

Operating on the left with D, we get

$$i\hbar\frac{\mathrm{d}}{\mathrm{d}t}|\Psi\rangle_{\mathrm{R}} = \left[D\hat{H}D^\dagger - i\hbar D\left(\frac{\mathrm{d}D^\dagger}{\mathrm{d}t}\right)\right]|\Psi\rangle_{\mathrm{R}}. \tag{2.13}$$

The term in brackets defines $\hat{H}_{\rm R}$, which when evaluated becomes

$$\hat{H}_{\rm R} = \frac{\hbar}{2}\begin{bmatrix} -\delta & \Omega_{eg}\mathrm{e}^{-i\phi} \\ \Omega_{eg}^{*}\mathrm{e}^{i\phi} & \delta \end{bmatrix}. \tag{2.14}$$

The eigenvalues $\lambda_{\pm}$ of $\hat{H}_{\rm R}$ are

$$\lambda_{\pm} = \pm\frac{\hbar\Omega_{\rm r}}{2}, \tag{2.15}$$

where the off-resonant Rabi frequency is defined as $\Omega_{\rm r} \equiv \sqrt{|\Omega_{eg}|^2 + \delta^2}$.

Since the overall phase of the quantum state is arbitrary, the initial phase ϕ is assumed to be combined with the phase of Ω_{eg} to make Ω_{eg} real and positive. Then the eigenstates of $\hat{H}_{\rm R}$ are given by (see, for example, Cohen-Tannoudji *et al.* [9])

$$\begin{aligned} |\lambda_{+}\rangle &= \cos(\tfrac{\theta}{2})|e\rangle_{\rm R}\mathrm{e}^{-i\phi/2} + \sin(\tfrac{\theta}{2})|g\rangle_{\rm R}\mathrm{e}^{i\phi/2} \\ |\lambda_{-}\rangle &= -\sin(\tfrac{\theta}{2})|e\rangle_{\rm R}\mathrm{e}^{-i\phi/2} + \cos(\tfrac{\theta}{2})|g\rangle_{\rm R}\mathrm{e}^{i\phi/2}, \end{aligned} \tag{2.16}$$

where θ is defined by the relations

$$\sin\theta = \Omega_{eg}/\Omega_{\rm r},\ \cos\theta = -\delta/\Omega_{\rm r},\ 0 \le \theta \le \pi. \tag{2.17}$$

With the Hamiltonian (2.9) the time evolution of the atom in the presence of the light is calculated by solving the eigenvector-eigenvalue problem and then writing the initial state in terms of a projection onto the new basis states, *i.e.*, the new eigenvectors. The time evolution of each of the eigenvectors is particularly simple: if $|\lambda_{+}\rangle$ is the eigenvector, then the time evolution is given by an oscillation about the eigenfrequency, $\mathrm{e}^{-i\lambda_{+}\tau/\hbar}|\lambda_{+}\rangle$. Thus, if at time t_0, the quantum state *in the rotating frame* is $|\Psi(t_0)\rangle_{\rm R}$, then

$$|\Psi(t_0+\tau)\rangle_{\rm R} = \left(\mathrm{e}^{-i\lambda_{+}\tau/\hbar}|\lambda_{+}\rangle\langle\lambda_{+}| + \mathrm{e}^{-i\lambda_{-}\tau/\hbar}|\lambda_{-}\rangle\langle\lambda_{-}|\right)|\Psi(t_0)\rangle_{\rm R}. \tag{2.18}$$

The time evolution for the general case of non-zero detuning $\delta \neq 0$ but constant laser amplitude has been worked out elsewhere [6, 8]. For the special case of $\delta = 0$, the effect of a pulse of light of duration τ on the atom is described by a simple 2×2 matrix

$$\hat{U}_{\rm R} = \begin{bmatrix} \cos\left(\frac{\Omega_{\rm r}\tau}{2}\right) & -i\mathrm{e}^{-i\phi}\sin\left(\frac{\Omega_{\rm r}\tau}{2}\right) \\ -i\mathrm{e}^{i\phi}\sin\left(\frac{\Omega_{\rm r}\tau}{2}\right) & \cos\left(\frac{\Omega_{\rm r}\tau}{2}\right) \end{bmatrix}. \tag{2.19}$$

From the form of the matrix $\hat{U}_{\rm R}$, one can readily see that an atom initially in the ground state, and exposed to two pulses of "area" $\int \Omega_{\rm r}(t)\mathrm{d}t = \Omega_{\rm r}\tau =$

$\pi/2$ will undergo the transformations

$$|\Psi\rangle = \begin{bmatrix} 0 \\ \\ 1 \end{bmatrix} \rightarrow \begin{bmatrix} -i/\sqrt{2} \\ \\ 1/\sqrt{2} \end{bmatrix} \rightarrow \begin{bmatrix} -i \\ \\ 0 \end{bmatrix}. \tag{2.20}$$

If the atomic oscillation during the drift time T in between the two $\pi/2$ pulses is the same as the microwave oscillator, the atom will be put into the excited state. If the number of oscillations differs by a π radians, the atom is left in the ground state. Thus, the interference creates an oscillation between the ground and excited state with an effective resonance linewidth of $\delta_{\mathrm{FWHM}} = \pi/T$. Note that this interference is strictly between two internal states of the atom.

The mathematical description of a two-level atom is identical to the description of a spin 1/2 system, where an atom in the ground state is depicted as a spin down Bloch vector aligned along the minus z-axis and an atom in the excited state is a spin up vector. The transformation given by equation (2.10) is equivalent to transforming into a frame of reference rotating at the laser frequency ω_{L}. In this frame of reference, if the laser frequency $\omega_{\mathrm{L}} = \omega_{eg}$, the excitation of an atom is depicted as a static torque in the $x-y$ plane. An excitation from the ground state to the excited state is depicted as a torque applied for a time needed to cause the Bloch vector to rotate by π radians from the spin down state to the spin up state. The relative phase of the atom with respect to the driving electric field is given by the angle between the projection of the Bloch vector and the torque vector on to the x-y plane. This geometric picture is often very useful in developing intuition about two-level atoms [7].

2.2 Interference due to different physical paths

We will now take the other extreme position and assume that the atom remains in one internal state and the interference is between parts of the atom that have taken two or more separate paths. Just as optical waves can be diffracted from matter gratings, matter waves can be diffracted from a optical grating defined as the periodic variations in the intensity of light field.

We again begin with the Schrödinger equation

$$-\left[\frac{\hbar^2}{2M}\nabla^2 - V(\mathbf{x},t)\right]\Psi(\mathbf{x},t) = i\hbar\frac{\partial\Psi}{\partial t}(\mathbf{x},t). \tag{2.21}$$

For $V(\mathbf{x},t) = V(\mathbf{x})$ independent of time, $\Psi(\mathbf{x},t) = \Psi(\mathbf{x})\exp(-iEt/\hbar)$ and the total energy $E = T + V$ is constant. Thus, we obtain the Helmholtz equation,

$$\nabla^2\Psi(\mathbf{x},t) + k^2\Psi(\mathbf{x},t) = 0, \tag{2.22}$$

with

$$k(\mathbf{x}) = \sqrt{\frac{2M}{\hbar^2}\left[E - V(\mathbf{x})\right]}. \tag{2.23}$$

We seek a solution to the Helmholtz equation of the form $\Psi(\mathbf{x}) \sim \mathrm{e}^{\mathrm{i}\psi(\mathbf{x})}$. Thus, $\psi(\mathbf{x})$ will satisfy

$$-(\nabla\psi)^2 + i\nabla^2\psi + k^2 = 0. \tag{2.24}$$

If the potential $V(r)$ is slowly varying relative to $1/k(r)$, then it is possible to define a local de Broglie wavelength $\lambda_{\mathrm{d}B} = 2\pi/k(\mathbf{x})$, and the solution of (2.24) may be approximated by expanding about the local position $\mathbf{x} = 0$

$$\psi(\mathbf{x}) = \psi(0) + \mathbf{k}(0)\cdot\mathbf{x} + \nabla k(0)\frac{x^2}{2} + \ldots \tag{2.25}$$

In the WKB approximation, we take only the first order term in the Taylor series expansion. By direct substitution, one can readily see that $\Psi(\mathbf{x}) \sim \mathrm{e}^{i\mathbf{k}\cdot\mathbf{x}}$. Adding the explicit time dependence, the local wave function for the external motion becomes a plane wave

$$\Psi(\mathbf{x}, t) = \mathrm{e}^{i(\mathbf{k}(\mathbf{x})\cdot\mathbf{x} - \omega t)}, \tag{2.26}$$

where the de Broglie energy $E = \hbar\omega$ is defined as the total energy of the atom. More generally, the external motion part of the wave function at two positions $(\mathbf{x_a}, t_a)$ and $(\mathbf{x_b}, t_b)$ are related by

$$\Psi(\mathbf{x}_b, t_b) = \mathrm{e}^{i\int(\mathbf{k}\cdot\mathrm{d}\mathbf{x} - \omega\,\mathrm{d}t)}\,\Psi(\mathbf{x}_a, t_a). \tag{2.27}$$

2.3 Path integral description of interference

Feynman's path integral approach to quantum mechanics [10], provides a natural framework for analyzing atom interferometers [12]. The time evolution of a state vector is described by a unitary operator

$$|\Psi(t_b)\rangle = U(t_b, t_a)\,|\Psi(t_a)\rangle\cdot \tag{2.28}$$

The wave function is the projection of this state vector onto the position basis and can then be written as

$$\begin{aligned}\Psi(x_b, t_b) &= \langle x_b|\Psi(t_b)\rangle = \langle x_b|U(t_b, t_a)|\Psi(t_a)\rangle \\ &= \int \mathrm{d}x_a \langle x_b|U(t_b, t_a)|x_a\rangle\langle x_a|\Psi(t_a)\rangle \\ &= \int \mathrm{d}x_a K(x_b, t_b; x_a, t_a)\Psi(x_a, t_a),\end{aligned} \tag{2.29}$$

where the function K is quantum propagator

$$K(z_b, t_b; x_a, t_a) \equiv \langle x_b | U(t_b, t_a) | x_a \rangle \tag{2.30}$$

that gives the amplitude for the particle starting at point (x_a, t_a) ending at point (x_b, t_b). Note that the wave function $\Psi(x_b, t_b)$ at the space time point (x_b, t_b) is due to the contributions from *all* points $(x_a, t_a), (x'_a, t'_a), (x''_a, t''_a, ...)$ that end up at point (x_b, t_b), and is analogous to Huygens principle in optics.

Feynman showed that the quantum propagator can be written as

$$K(x_b, t_b; x_a, t_a) = \mathcal{N} \sum_{\Gamma} \mathrm{e}^{-iS/\hbar}, \tag{2.31}$$

where S is the action given by

$$S = \int_{t_a}^{t_b} L(x, \dot{x})\, \mathrm{d}t. \tag{2.32}$$

$L(x, \dot{x})$ is the Lagrangian of the atomic path, $\mathcal{N}$ is the normalization factor, and the sum is over *all* paths connecting point (x_a, t) to point (x_b, t). In the sum over all states, if $S_{\mathrm{Cl}} \gg \hbar$, then slight changes in the path will give an amplitude with a wildly different phase. Only the paths near an extremum, *i.e.*, the classical trajectory, will allow the phases to add constructively. In the limit of a large action, the sum in (2.31) simplifies and the wavefunction is simply

$$\Psi(x_b, t_b) = \mathrm{e}^{iS_{\mathrm{Cl}}/\hbar} \Psi(x_a, t_a). \tag{2.33}$$

In classical Lagrangian dynamics, the Hamiltonian is defined as

$$H_{\mathrm{Cl}} \equiv p\dot{x} - L_{\mathrm{Cl}}. \tag{2.34}$$

By substituting (2.34) into (2.32), we recover (2.27).

2.4 Atom optics

Atom optics and photon optics both satisfy the Helmholtz equation and their phase properties are described by strikingly similar equations. To push the analogy further, equations (2.22) and (2.23), tell us that a static potential acts as a medium with an effective refractive index of

$$n(\mathbf{x}) = \frac{k(\mathbf{x})}{k_0} = \sqrt{\left(1 - \frac{V(\mathbf{x})}{E}\right)} \tag{2.35}$$

where $k_0 = \sqrt{(2ME/\hbar^2)}$.

There are some important differences. For example, atomic de Broglie waves are inherently dispersive, whereas photons propagate in vacuum non-dispersively. Using the definitions for phase velocity, $k \equiv \omega/v_{\mathrm{P}}$ and $v_{\mathrm{G}} \equiv \partial\omega/\partial k$, we have

$$v_{\mathrm{P}} = \frac{1}{\hbar}\frac{E}{k} = \frac{\hbar k_0^2}{2Mk} = \frac{1}{n}\sqrt{\frac{E}{2M}}, \tag{2.36}$$

$$v_{\mathrm{G}} = \frac{1}{\hbar}\frac{\partial E}{\partial k} = \frac{\hbar k}{M} = n\sqrt{\frac{2E}{M}}\,. \tag{2.37}$$

The group velocity v_{G} is identified with the wave packet velocity while the velocity of the phase fronts v_{P} are associated with (2.33). Note that the product $v_{\mathrm{P}}v_{\mathrm{G}}$ is independent of n.

As a simple application of the atom optics formalism, consider a wave packet moving along the z-direction and incident onto a parabolic potential along the x-axis. If $V < 0$, the index of refraction $n > 1$, and the potential focuses the wave packet. Using the Feynman propagator description of quantum mechanics, one traces out each of trajectories for each space time point $(\mathbf{x}, t)$. As each part of the wave packet traverses through the "thin lens" defined by this potential, each path receives an impulse $F\delta t$ that is linearly proportional to the lateral displacement from the center of the lens. In the paraxial approximation, these impulses cause all of the particle trajectories to converge at the "focal point" of the lens.

One can also understand why the de Broglie wave has to be dispersive. Since $k > k_0$ in the region where $V < 0$, the shorter wavelength delays the number of cycles of phase at some point past the potential. Similarly, the part of the atom that goes through the center of the lens will arrive sooner since particles increase their speed when they roll into a potential well.

In real experiments, we do not have plane waves and one must consider wave packets with a finite velocity spread. For many types of atom interferometers, this velocity spread poses serious limitations on the fringe visibility analogous to finite longitudinal and spatial coherence of a light source in optical interferometers [11]. As an example, consider a Young's double slit interferometer. Assume a single slit (or series of slits) creates a beam of atoms propagating in the x-direction with negligible spatial incoherence, but the thermal beam has a momentum spread

$$\Psi(\mathbf{x}, t) = \int_{-\infty}^{+\infty} \frac{\mathrm{d}\mathbf{k}}{(2\pi)^3}\, a_k\, \exp[i(\mathbf{k}\cdot\mathbf{x} - E_k t/\hbar)]. \tag{2.38}$$

We are implicitly assuming that the atomic system can be described by a coherent wave packet, and take as a example, a_k as given by

$$a_k = \frac{(4\pi)^{1/4}}{\sigma_k^{1/2}} \exp[-(k-k_0)^2/2\sigma_k^2]. \tag{2.39}$$

The wave packet will move with a group velocity $v_{\rm G} = \hbar k_0/M$ and expand with a free space dispersion given by $E_k = \hbar^2 k^2/2M$. After a time t, it will have expanded to

$$\sigma_x^2(t) = \frac{1}{\sigma_k^2} + \frac{\hbar^2 t^2}{M^2}\sigma_k^2. \tag{2.40}$$

At a distance L further down stream from the double slit, a detector records the arrival of atoms at different positions y normal to the slits. At the slit, the phases of the two wave packets overlap perfectly, but at a position y the wave packets are longitudinally displaced from each other by $\pm l = d/\mathrm{Ly}$. The probability to detect an atom at position y is proportional to

$$\int |\Psi(x-l,t) + \Psi(x+l,t)|^2 \,\mathrm{d}x\,. \tag{2.41}$$

For our Gaussian wave packet, the interference term is

$$\int \Psi^*(x-l,t)\,\Psi(x+l,t)\,\mathrm{d}x = \frac{1}{4}\exp\left(-\sigma_k^2 l^2\right)\exp\left(2ik_0 l\right). \tag{2.42}$$

Note that there is no time dependence in (2.42), so that the quantum spreading wave packet does not affect the interference pattern.

This result is general and holds even if the atomic source is a statistical mixture of random phases. The reason is because any pair of wavefunctions that time evolve together undergo the same unitary transformation $U(t) = \mathrm{e}^{-iHt/\hbar}$ and

$$\langle\Psi_1(t)|\Psi_2(t)\rangle = \langle\Psi_1(0)|U(t)^\dagger U(t)|\Psi_2(0)\rangle = \langle\Psi_1(0)|\Psi_2(0)\rangle\,\cdot \tag{2.43}$$

The intensity at the position y is then proportional to

$$I(y) = |\Psi_{\Gamma_1} + \Psi_{\Gamma_2}|^2 = \frac{I_0}{2}\left[1 + \exp\left(-\frac{\sigma_k^2 d^2}{4L^2}y^2\right)\cos\left(\frac{k_0 d}{L}\right)y\right]. \tag{2.44}$$

The fringe visibility fades with the longitudinal separation of the two wave packets $\pm\delta x = d/(2\,\mathrm{Ly})$

$$\mathcal{V}(\delta x) \equiv \frac{I_{\max} - I_{\min}}{I_{\max} + I_{\min}} = \exp\left(-\sigma_k^2\,\delta x^2\right). \tag{2.45}$$

Thus, the interference fringes will begin to disappear as soon as the center of mass wave packet separation begins to exceed the coherence length $l_{\rm coh} = 1/\sigma$. While the spatial overlap arising from dispersion is a necessary condition for observing interference, it is not sufficient. We shall see that optical pulse beam splitters do not have this limitation and are far more tolerant of both spatial and longitudinal coherence.

2.5 Interference with combined internal and external degrees of freedom

The formalism presented in Section 2.1 was originally developed for rf and microwave excitation. In those cases, the lateral dimensions of an atomic beam are much smaller than the wavelength of the electromagnetic waves. Consequently, all atoms passing through two traveling microwave fields will interact with nearly the same relative phase. Furthermore, the position of the atoms can be decoupled from the internal states and is considered to be a classical variable.

If one applies the Ramsey technique to the optical domain, the spatial variation of the electric field and the momentum recoil of the atom when it absorbs a photon has to be considered. Also, the spatial extent of the atomic source and the spread of transverse momenta have to be included. For example, imagine an atomic wave packet irradiated by a $\pi/2$ pulse that generates two packets. The two packets will begin to diverge with some recoil velocity, and at some later time, the two wave packets may no longer overlap when the second $\pi/2$ pulse is applied. If this is the case, Ramsey fringes will not be observed. Alternatively, an atomic source with very low transverse velocity spread would have atoms with de Broglie wavelengths that exceed the wavelength of the light. In this case, the semiclassical approximation breaks down and the "position of the atom" relative to a particular crest of the wave has no meaning.

One approach to analyzing atom interferometers is to consider explicitly the propagation of spatial wave packets as in Section 2.2. In this approach, the interferometer phase shifts are calculated combining a set of phase-shift rules for the atom-light interaction points with the phase shifts associated with the free-space propagation [4, 13, 14, 16]. These results have been generalized to account for AC Stark shifts in two-photon transitions by Weiss *et al.* [15].

As an alternate approach to the wave-packet description of the atomic trajectories, one can begin with a quantum treatment where the atomic wave packets are taken to be the sum of momentum plane-wave states. The momentum transfer due to the interaction of the electromagnetic field (*e.g.*, single-photon absorption, stimulated Raman transition, or adiabatic transfer) are calculated for a given plane-wave component and the integral over all of the momentum states in the atomic ensemble is performed last. In this basis, each of the atomic states is described in terms of a tensor product of the Hilbert space describing the internal energy state of the atom and the Hilbert space describing the external degrees of freedom,

$$\begin{aligned} |e, \mathbf{p}_e\rangle &= |e\rangle \otimes |\mathbf{p}_e\rangle, \\ |g, \mathbf{p}_g\rangle &= |g\rangle \otimes |\mathbf{p}_g\rangle. \end{aligned} \tag{2.46}$$

The Hamiltonian becomes

$$\hat{H} = \frac{\hat{\mathbf{p}}^2}{2m} + \hbar\omega_e|e\rangle\langle e| + \hbar\omega_g|g\rangle\langle g| - \mathbf{d}\cdot\mathbf{E} \tag{2.47}$$

where $\hat{\mathbf{p}}$ operates on the momentum portion of the basis states. The interaction term is modified to include the spatial dependence of the electric field

$$\mathbf{E} = \mathbf{E}_0\cos(\mathbf{k}\cdot\mathbf{x} - \omega_{\mathrm{L}}t + \phi). \tag{2.48}$$

The new terms of the electric field operator, $\mathrm{e}^{i\mathbf{k}\cdot\mathbf{x}}$ can be rewritten with the closure relation

$$\begin{aligned} 1\cdot\mathrm{e}^{\pm i\mathbf{k}_{\mathrm{L}}\cdot\mathbf{x}} &= \int \mathrm{d}^3\mathbf{p}\,\mathrm{e}^{\pm i\mathbf{k}_{\mathrm{L}}\cdot\mathbf{x}}|\mathbf{p}\rangle\langle\mathbf{p}| \\ &= \int \mathrm{d}^3\mathbf{p}\,|\mathbf{p}\pm\hbar\mathbf{k}_{\mathrm{L}}\rangle\langle\mathbf{p}|. \end{aligned} \tag{2.49}$$

The last step in equation (2.49) uses the fact that $\mathrm{e}^{\pm i\mathbf{k}_{\mathrm{L}}\cdot\mathbf{x}}$ is the translation operator of the momentum eigenstate $|\mathbf{p}\rangle$. We see explicitly how the spatial dependence of the electric field in the momentum basis formally gives us the well known result: the absorption or emission of a photon of wave vector $\mathbf{k}$ changes the atom's total momentum from $\mathbf{p}$ to $\mathbf{p}+\hbar\mathbf{k}_{\mathrm{L}}$. This one-to-one correspondence between the internal and external degrees of freedom implies that the basis states simplify to $|g,\mathbf{p}\rangle$ and $|e,\mathbf{p}+\hbar\mathbf{k}_{\mathrm{L}}\rangle$ for each momentum $\mathbf{p}$.

Following the development of the Ramsey case without photon recoil, equation (2.9), we transform into the rotating frame and use the rotating wave approximation (different "rotations"!), to get the Hamiltonian

$$\hat{H}_{\mathrm{R}} = \left\{ \frac{\hat{\mathbf{p}}^2}{2M} + \frac{\hbar}{2}\begin{bmatrix} -\delta & \Omega_{eg}\,\mathrm{e}^{i(\mathbf{k}_{\mathrm{L}}\cdot\mathbf{x})-\phi)} \\ \Omega^*_{eg}\mathrm{e}^{-i(\mathbf{k}_{\mathrm{L}}\cdot\mathbf{x}-\phi)} & \delta \end{bmatrix} \right\}. \tag{2.50}$$

The time evolution of the ket can be written in terms of slowly varying coefficients $c_{e,\mathbf{p}+\hbar\mathbf{k}}(t)$ and $c_{g,\mathbf{p}}(t)$

$$|\Psi(t)\rangle = \begin{bmatrix} c_{e,\mathbf{p}+\hbar\mathbf{k}}(t)\mathrm{e}^{-i\left(\omega_e+\frac{|\mathbf{p}+\hbar\mathbf{k}|^2}{2M\hbar}\right)t} \\ \\ c_{g,\mathbf{p}}(t)\mathrm{e}^{-i\left(\omega_g+\frac{|\mathbf{p}|^2}{2M\hbar}\right)t} \end{bmatrix}. \tag{2.51}$$

The detuning now has additional terms

$$\delta = \omega_{\mathrm{L}} - \left(\omega_{eg} + \frac{\mathbf{p}\cdot\mathbf{k}}{M} + \frac{\hbar|\mathbf{k}|^2}{2M}\right) \tag{2.52}$$

corresponding to the Doppler shift $\mathbf{p}\cdot\mathbf{k}_{\rm L}/M$ and the photon-recoil shift $\hbar|\mathbf{k}_{\rm L}|^2/2M$.

When a photon of momentum $\hbar\mathbf{k}$ puts an atom into a coherent superposition of two energy states, the recoil will cause the parts of the atom in each of its internal states $|g\rangle$ and $|e\rangle$ to separate with a velocity $\mathbf{v}_{\rm r}=\hbar\mathbf{k}_{\rm L}/M$. If these two wave packets are to interfere at some later time, they must be made to spatially overlap. If optical photons are used in an atomic fountain, the recoil distance can approach a centimeter, much larger than the spatial coherence of the atomic source. Thus, the application of equations (2.9) as modified by equations (2.51) and (2.52) must also consider the spatial overlap of wave packets. As a simple example, the simple Ramsey $\pi/2-\pi/2$ pulse sequence will not produce interference fringes.

More complicated pulse sequences are needed to bring the parts of the atom, which separate during the first $\pi/2$ pulse, back together again at some later time. The simplest optical pulse sequence that recombines the atomic wave packets is the $\pi/2-\pi-\pi/2$ pulse sequences shown in Figure 1a, and first demonstrated by Kasevich and Chu [4,17]. The first $\pi/2$ pulse acts as a beam splitter, introducing a velocity difference $\mathbf{v}_{\rm r}=\hbar\mathbf{k}/m$ between the two wave packets. After a time T, the π pulse acts as a mirror and redirects the two wave packets so that they overlap at the time $2T$ of the second $\pi/2$ pulse. The momentum states making an atomic transition will receive that same momentum transfer and thus register the same net interferometer phase shift for this pulse sequence. This is true even if the inhomogeneous velocity distribution is sufficiently broad that the spectral width of the π pulse ($\delta\omega\simeq 1/\tau$) is less than the Doppler-broadened linewidth.

This statement is proved rigorously using the formalism presented here. We use equation (2.50) to analyze a $\pi/2-\pi-\pi/2$ pulse sequence. The result for $\delta=0$ is that we recover equation (2.19). To generalize the result slightly, we now take $0<|\delta|\ll\Omega_{\rm r}$, so that $\cos\theta\simeq 0$ and $\sin\theta\simeq 1$. For a more complete treatment including small deviations from ideal pulse areas and detunings that cause AC Stark shifts, see Weiss *et al.* [15]. The unitary Bloch rotation operator $\hat{U}$ becomes

$$\hat{U}_{\rm R}=\begin{bmatrix} {\rm e}^{-i\delta\tau/2}\cos\left(\frac{\Omega_{\rm r}\tau}{2}\right) & -i{\rm e}^{-i\delta\tau/2}{\rm e}^{-i(\delta t_0+\phi)}\sin\left(\frac{\Omega_{\rm r}\tau}{2}\right) \\ -i{\rm e}^{i\delta\tau/2}{\rm e}^{i(\delta t_0+\phi)}\sin\left(\frac{\Omega_{\rm r}\tau}{2}\right) & {\rm e}^{i\delta\tau/2}\cos\left(\frac{\Omega_{\rm r}\tau}{2}\right) \end{bmatrix}. \tag{2.53}$$

Consider an atom initially in $|g,\mathbf{p}\rangle$. A crucial component of light-pulse atom interferometers is the phase of the atom relative to the driving fields. Suppose that the laser detuning δ is constant for the entire pulse sequence and phase ϕ for each pulse may vary. We will later show in Section 3.2.2 that phase shifts accrued during the time the light is off are the same for each path. Successive applications of (2.53) for a $\pi/2$ pulse at t_1, a π pulse

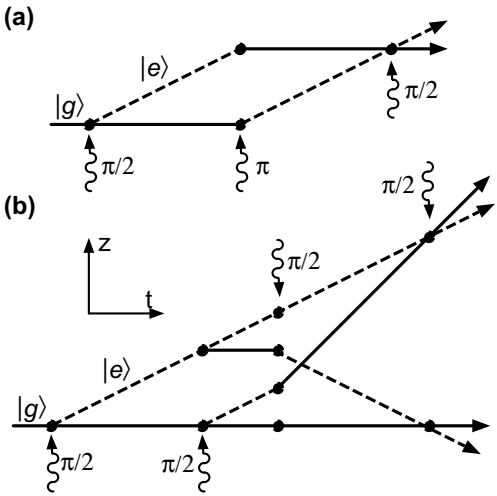

Fig. 1. Recoil diagrams for two optical pulse atom interferometers. The vertical axis is the position z of an atom relative to a reference frame freely falling along the initial trajectory of the atom. Solid and dashed lines indicate paths for which the atom is in $|g\rangle$ and $|e\rangle$, respectively. The vertices are points of interaction with light pulses, with $\mathbf{k}_{\rm eff}$ indicated by the direction of the arrows. (a) The $\pi/2 - \pi - \pi/2$ geometry used for the g measurement. (b) The Ramsey-Bordé sequence used for the photon recoil measurement. Note that the orientation of $\mathbf{k}_{\rm eff}$ is reversed for the second pair of $\pi/2$ pulses.

at $t_2 = T + \tau/2 + t_1$ and a $\pi/2$ pulse at $t_3 = 2T + 3\tau/2 + t_1$ yields

$$c_{e,\mathbf{p}+\hbar\mathbf{k}}(t_3 + \tau/2) = -\frac{i}{2}\mathrm{e}^{-i\delta\tau/2}\mathrm{e}^{-i[\delta t_2 + \phi(t_2)]}\left(1 - \mathrm{e}^{i\delta\tau/2}\mathrm{e}^{-i\Delta\phi}\right), \qquad (2.54)$$

where

$$\Delta\phi = \phi(t_1) - 2\phi(t_2) + \phi(t_3). \qquad (2.55)$$

At each time t_i, $\phi(t_i)$ is the phase of the light relative to the atom, referenced to the phase at some fixed time point. The probability of finding the atom in the excited state is

$$|c_{e,\mathbf{p}+\hbar\mathbf{k}}(2T + 2\tau)|^2 = \frac{1}{2}\left[1 - \cos\left(\Delta\phi - \delta\tau/2\right)\right]. \qquad (2.56)$$

Note that $\Delta\Phi \equiv \Delta\phi - \delta\tau/2$ is not a function of the momentum so that atoms (or parts of one atom) in different momentum states will contribute coherently to the interference signal. Consequently, the phase shift of a sum over a large number of momentum states (*i.e.*, a wave packet), will be

given by this equation. For the pulse times given above, if the atoms see a constant detuning and if the phase of the driving light field is not changed, then $\Delta\Phi = \delta\tau/2$, so by equation (2.56), the atom will be found in the ground state after the last pulse. The atomic population will be modulated if the relative phase of the pulses relative to the atoms is changed. This effect is the basis for inertial force measurements and the photon recoil measurement described in the following sections.

This pulse sequence was first used in nuclear magnetic resonance (NMR) studies to compensate for the inhomogeneous spread of resonance frequencies in the NMR sample. Nuclear spins sitting at different sites of a solid have different resonance frequencies. If a $\pi/2 - \pi/2$ pulse sequence is used, the inhomogeneous spread of frequencies would wash out the fringes. On the other hand, a π pulse sandwiched in between the two $\pi/2$ pulses would cause the spins to re-phase. In the absence of the second $\pi/2$ pulse, a pulse would be emitted from the sample in the form of a "spin echo". When applied to atom interferometry, this pulse sequence does an equivalently beautiful thing: it compensates for the inhomogeneous velocity width of the atomic sample so that the fringe visibility does not require exceptionally high longitudinal or spatial coherence.

In terms of the Feynman formulation of quantum mechanics, a sample of atoms with a spread of momentum states will have many wavefunctions at space-time points $\Psi(\mathbf{x_a}, t_a), \Psi(\mathbf{x_a}', t_a'),...$ contributing to the wavefunction $\Psi(\mathbf{x_b}, t_b)$, since each of the different space time points $(\mathbf{x_a}, t_a), (\mathbf{x_a}', t'),...$ with different momenta can end up at point $(\mathbf{x_b}, t_b)$. The phase difference of all of these paths are the same, even in the presence of a uniform gravitational field. Thus, this type of atom interferometer can produce almost 100% fringe visibility, even with mediocre longitudinal coherence. As compared with interferometers based on microstructures which require high longitudinal coherence, optical pulse interferometers have higher fringe contrast with simultaneously higher atom fluxes.

The first optical pulse interferometer considered used a pulse sequence consisting of one pair of $\pi/2$ pulses followed by a pair of oppositely directed $\pi/2$ pulses as shown in Figure 1b is another pulse scheme used to redirect the trajectories of the atoms [18,19]. This pulse sequence was originally used to extend the Ramsey separated oscillatory field technique to the optical domain for the purpose of constructing an optical clock. Eight years later, Bordé realized that this pulse sequence generates an atom interferometer with spatially separated wave packets [20]. We have used this pulse sequence to measure the recoil velocity of an atom which then yields a value for $\hbar/m$ [15,21]. The analysis of this pulse sequence is very similar to the analysis for the $\pi/2 - \pi - \pi/2$ sequence. The details of this type of interferometer will be discussed in Section 5.

3 Beam splitters and interferometers

The heart of any interferometer are the beam splitters. These components have to divide each atom into a superposition of (at least) two coherent states and then return the two parts back together while maintaining the quantum coherence. A number of coherent beam splitters have been demonstrated, ranging from micro fabricated structures, crystalline or magnetically patterned surfaces, standing waves and optical pulses of light.

3.1 Interferometers based on microfabricated structures

A key technology used in the demonstration of these types of interferometers was the ability to fabricate free-standing diffraction gratings. Silicon nitride gratings (now commercially available) on the order of $100-200$ nm thick and with a 200 nm period can be made with better than 10 nm accuracy over an area of 0.8 mm $\times$ 0.8 mm. The primary advantage of an interferometer based on physical transmissions gratings is that the same gratings will work for any atom or molecule.

A serious disadvantage is the low atom throughput. The theoretical maximum fringe contrast for an atom interferometer using three equally spaced transmission diffraction gratings (obtained by optimizing the open fraction of the gratings) is 67%, provided one uses a very well collimated atomic beam. Up to 50% fringe contrast has been observed, but in order to achieve this contrast, the aperture sizes have to be chosen so that only $\leq 1\%$ of collimated atomic beam detected [22]. This disadvantage has prompted Clauser [23] and to consider another class of interferometers that use physical gratings, but depend on the so-called "Talbot-Lau" effect instead of the better-known Fraunhofer diffraction. In a first version of the Talbot interferometer, the atomic current was demonstrated to be orders of magnitude higher for a given source brightness [23].

In the case of transmission gratings, the atom is either adsorbed by the grating or left alone, so that the sole effect of the grating is to impress a spatial modulation on the wave function that only modifies the external degrees of freedom of the state vector. In the case of an optical potential, the atom can make a transition to another internal quantum state. (This aspect of atom interferometry is not an issue with photons, electrons or neutrons.)

Since matter waves and optical waves are both described by the same Helmholtz equation (2.22) with k-vector defined as (2.23), the diffraction of matter waves and light by microstructures are essentially equivalent. However, we will use a description of matter wave interferometer [24] that departs from the usual description found in standard electromagnetic text books in order to introduce the Talbot-Lau effect.

Consider an atom wave propagating in the z direction that is partially masked by a diffraction grating with some periodic structure $\eta(x) = \eta(x+a)$, where a is the period of the grating. Immediately after passing through the grating, the wavefunction $\Psi(x) = \eta(x)$, which can be written as the sum of plane wave states

$$\Psi(x) = \eta(x) = \sum_k \eta_k \mathrm{e}^{-ikx}. \tag{3.1}$$

Translational symmetry $\eta(x) = \eta(x \pm na)$ with n an integer demands that

$$\sum_k \eta_k \mathrm{e}^{-ikx} = \sum_k \eta_k \mathrm{e}^{-ik(x+na)} = \sum_k \eta_k \mathrm{e}^{-ikx} \mathrm{e}^{-inka}. \tag{3.2}$$

For this statement to be true for all x and $\pm na$, k must take on integer values $k = nG = (2\pi/a)n$. $G = 2\pi/a \sim k_\mathrm{L}$ is sometimes referred to as the "reciprocal lattice vector". Thus,

$$\eta(x) = \sum_n \eta_n \mathrm{e}^{ink_\mathrm{L}x}. \tag{3.3}$$

We rewrite this expression by multiplying both sides by $\mathrm{e}^{-ikx}/\sqrt{2\pi}$ and integrating over all space to get

$$\begin{aligned}
\tilde{\Psi}(p) &= \frac{1}{\sqrt{2\pi}} \int_{-\infty}^{+\infty} \eta(x) \mathrm{e}^{-ikx} \mathrm{d}x \\
&= \frac{1}{\sqrt{2\pi}} \sum_n \eta_n \int_{-\infty}^{+\infty} \mathrm{e}^{i(nk_\mathrm{L}-k)x} \mathrm{d}x \\
&= \frac{1}{\sqrt{2\pi}} \sum_n \eta_n [2\pi\delta(nk_\mathrm{L} - k)] \\
&= \sqrt{2\pi}\, \eta_k.
\end{aligned} \tag{3.4}$$

Equation (3.4) tells us that the momentum distribution and hence, the diffraction pattern at infinity, is the Fourier transform of the aperture transmission function. This result is the well-known Fraunhofer approximation to the Fresnel-Kirchhoff diffraction integrals.

Note that we assumed the periodic lattice only changed the momentum component along x, normal to the atomic beam and the momentum component in the z direction remains unchanged and $k_z \gg k_x$. This approximation is sometimes referred to as the "Raman Nath" or "thin grating" regime. It is valid if the interaction time τ_int with the beam splitter is short and energy has to be conserved to the extent that $\Delta E \leq \hbar/\tau_\mathrm{int}$. Equation (3.4) tells us that a large number of momentum states are populated after the interaction. For long interaction times, energy must be conserved

and the atoms scatter predominantly into one diffraction order. This "thick grating" regime is also known as Bragg scattering.

Combining (3.1) and (3.4), the Fourier transform of $\Psi(x)$ is given by

$$\tilde{\Psi}(p) = \sqrt{2\pi\hbar} \sum_n \eta_n \, \delta(p - m\hbar k), \tag{3.5}$$

where

$$\eta_n = \int \frac{\mathrm{d}x}{a} \, \mathrm{e}^{-imkx} \, \eta(x) \tag{3.6}$$

is the Fourier coefficient.

One way to derive an expression for the interference pattern some distance downstream from the microstructure grating is convert displacement into a time evolution of the system expressed in a convenient basis set. The classical motion of the atoms in the z direction gives us the needed correspondence between distance and the time.

$$t = z/u, \tag{3.7}$$

where $u = p_z/M$ and M is the atomic mass. For each u, we use equation (3.4) to get the time evolution of the momentum space wave function

$$\tilde{\Psi}(p,t) = \mathrm{e}^{-i\epsilon_\mathrm{p} t/\hbar} \, \tilde{\Psi}(p) = \sqrt{2\pi\hbar} \sum_m \eta_m \, \exp[-im^2\omega_k t] \, \delta(p - m\hbar k), \tag{3.8}$$

where $\epsilon_\mathrm{p} = p^2/2M$ is the kinetic energy of an atom with momentum p. We see that the periodic grating constraints the time evolution to occur as multiples of m^2 of the recoil frequency $\omega_\mathrm{r} = \hbar k^2/2M$.

In the space representation,

$$\begin{aligned} \Psi(x,t) &= \int_{-\infty}^{+\infty} \frac{\mathrm{d}k}{\sqrt{2\pi}} \, \mathrm{e}^{ikx} \, \tilde{\Psi}(p,t) \\ &= \sum_m \eta_m \, \exp[\mathrm{i}mkx - \mathrm{i}m^2\omega_\mathrm{r} t]. \end{aligned} \tag{3.9}$$

The interference of the various amplitudes in (3.9) as a function of the time t or the distance x was first predicted by Chebotayev *et al.* [25] and observed by Chapman *et al.* [26].

After a "Talbot" time $t_\mathrm{T} \equiv 2\pi/\omega_\mathrm{r}$ or "Talbot" distance $L_\mathrm{T} \equiv ut_\mathrm{T} = 2d^2/\lambda_{\mathrm{d}B}$, the atomic wave function rephases to produce an image of the amplitude function of the transmission grating. This effect is discovered in optics by Talbot in 1836. One can also show [24] that a self-image of the grating, shifted along x by half a period, appears at distances $L_\mathrm{T}/2$. At distances L_T/n higher order atomic gratings are formed.

So far our analysis of these diffraction effects tacitly assumed that the angular divergence $\theta_{\rm b}$ of the atomic beam is less than $a/L_{\rm T}$, where a is the grating period. Otherwise the diffraction patterns associated with the different velocity sub-groups would wash out the overall diffraction pattern. For typical beams, this corresponds to $\theta_{\rm b} < 10^{-4}-10^{-5}$ rad. It is possible to circumvent this restriction and increase the usable beam flux by employing an "echo-like" technique analogous to the spin echo techniques used in NMR.

The "spin-echo" technique is based on an atomic beam passing through two identical diffraction gratings separated by a distance L. It turns out that the combined quantum diffraction and geometrical shadowing give a dephasing and rephasing which are unchanged from the classical case. Thus, this type of interferometer should be able to allow a less collimated (and hence higher flux) beam to be used [27]. The higher periodicities increase the interferometer sensitivity, but at the expense of fringe contrast. For further details, the reader is referred to the references cited in this section.

3.2 Interferometers based on light-induced potentials

3.2.1 Diffraction from an optical standing wave

Next, we consider an atomic beam propagating along the **z**-axis entering an optical standing wave

$$E_{\rm L} = E_0(z)\,\cos(k_{\rm L}x + \pi/4)\,\cos\omega_{\rm L}t. \tag{3.10}$$

As in Section 3.1, we will assume that the atomic kinetic energy is large compared with the atom-light interaction energy. Under these conditions, the group velocity of the packet remains constant and the change in z is turned into a time dependence $t = u/z$. The interaction Hamiltonian (2.50) then becomes

$$\hat{H}_{\rm R} = \frac{\hbar}{2}\begin{bmatrix} -\delta & \Omega_{eg}(t)\,\cos(k_{\rm L}x + \pi/4) \\ \Omega_{eg}(t)^*\,\cos(k_{\rm L}x + \pi/4) & \delta \end{bmatrix}. \tag{3.11}$$

Analogous to (2.15), the new eigenstates ("dressed states") have energies

$$\begin{aligned} U_{\pm}(x,t) &= \pm\frac{\hbar}{2}\sqrt{\delta^2 + \Omega_{eg}^2(t)\,\cos^2(k_{\rm L} + \pi/4)} \\ &\sim \pm\frac{\delta}{2} \pm \frac{\Omega_{eg}^2(t)}{4\delta}\,(1 - \sin 2k_{\rm L}z), \end{aligned} \tag{3.12}$$

where the last step is for detunings where $\delta \gg \Omega_{eg}$. Under these circumstances, an atom in the ground state $|g\rangle$ will evolve adiabatically into one of the dressed states $|\pm, n(\mathbf{x})\rangle$ which now has its de Broglie frequency ω modulated by the optical potential. After the atom passes through the standing

wave potential, its wave function acquires a phase shift given by

$$\begin{aligned}\Psi(x) &= \Psi_0 \exp\left(-i\int_t U_{+,n}(x,t')\mathrm{d}t'/\hbar\right) \\ &\sim \Psi_0' \exp\left(i\frac{\Omega_{eg}^2}{4\delta}\sin(2k_{\mathrm{L}}zt)\right). \end{aligned} \tag{3.13}$$

Once we know the real space wave function $\Psi(x)$, the momentum distribution (or in the real space amplitude in the Fraunhofer diffraction limit) is given by the Fourier transform of $\Psi(x)$. This type of diffraction was first demonstrated by Pritchard and collaborators [22, 28].

3.2.2 Interaction of atoms with light in the sudden approximation

In the previous section, we saw how a plane wave incident on a standing wave will have its phase spatially modulated by an optical potential. The differences in the phase were caused by the adiabatic evolution (3.13) of an atom from $|g\rangle$, to the dressed state $|+,n\rangle$, and then back to the initial state $|g\rangle$.

Beamsplitters based on optical pulses can be considered to be at the other extreme: the application of a potential in the sudden approximation. An atom in state $|g\rangle$ is suddenly irradiated with an optical field. In order to calculate the time evolution of the system, we project the initial state onto the new eigenstates (the dressed states) of the system, which in turn evolve in time as described in equations (2.18) and (2.19). The Rabi oscillations between excited and ground states are due to the interference between the two dressed states which experience different potentials and propagate with different phase and group velocities.

In atom interferometry, the motion of the atom with respect to the phase of the light inducing the transition is at the heart of the calculation of the fringe pattern. At the most basic level, consider a fixed atom irradiated by two Ramsey pulses separated by a time t. The atomic phase that accrues during that time is $\phi_{\mathrm{atom}} = \phi_e - \phi_g = \omega_{eg}t$. In the Ramsey technique, one compares this phase with the optical phase ϕ_{L}. If the atom has moved by a distance Δz in the same direction as the radiation, the number of cycles of phase the atom will see will be decreased by an amount $\Delta\phi_{\mathrm{L}} = k_{\mathrm{L}}\Delta x$.

We account for this change in phase due to the motion of the atom in the Feynman description quite easily since one evaluates the interaction at each space time point. By applying equations (2.19) and (2.53), the phase term ϕ includes the position (x_1, t_1) of the interaction by adding a phase term $k_{\mathrm{L}}x_1 - \omega_{\mathrm{L}}t_1$. Thus, we derive a simple rule for each interaction with an optical pulse: the atomic wave function is multiplied by one of four factors

depending on the transition.

$$\begin{array}{ll} \text{transition} & \text{multiplying factor} \\ |g\rangle \to |e\rangle & U_{eg}\ \exp[-i(k_{\mathrm{L}}x_1 - \omega_{\mathrm{L}}t_1 - \phi)] \\ |e\rangle \to |g\rangle & U_{ge}\ \exp[+i(k_{\mathrm{L}}x_1 - \omega_{\mathrm{L}}t_1 - \phi)] \\ |g\rangle \to |g\rangle & U_{gg} \\ |e\rangle \to |e\rangle & U_{ee}. \end{array} \tag{3.14}$$

The transition amplitudes U_{eg}, U_{ge}, U_{ee} and U_{gg} are determined by the pulse areas as given in unitary operator (2.53).

As an example of how one calculates the interference fringe pattern for an optical pulse interferometer, explicitly including the displacement of the atom, we calculate the phase shift for a $\pi/2 - \pi - \pi/2$ pulse sequence. It is clear that the phase shifts due to the free propagation

$$\delta\phi = S_{\mathrm{Cl}}/\hbar = \frac{1}{\hbar}\int_{\Gamma} \mathrm{d}t \left[\frac{1}{2}Mv^2\right] \tag{3.15}$$

are the same for both paths, due to the symmetry of the interferometer.

Referring to Figure 2 we apply the transition rules to path I to calculate the amplitude for being in the state $|g\rangle$ at time t_3:

$$\begin{aligned} \Psi(x_3, t_3)|_{\Gamma_{\mathrm{I}}} = U_{gg}U_{ge}\ &\exp\{+i[k_{\mathrm{L}}x_{2,I} - \omega t_2 - \phi_2]\} \\ &\times U_{eg} \exp\{-i[k_{\mathrm{L}}x_1 - \phi_1]\}\ \Psi(x_1, t_1). \end{aligned} \tag{3.16}$$

Similarly, for path II, the amplitude is

$$\begin{aligned} \Psi(x_3, t_3)|_{\Gamma_{\mathrm{II}}} = U_{ge} &\exp\{+i[k_{\mathrm{L}}x_3 - \omega t_3 - \phi_3]\} \\ &\times U_{eg}\ \exp\{-i[k_{\mathrm{L}}x_{2,II} - \omega t_2 - \phi_2]\} \\ &\times U_{gg}\, \Psi(x_1, t_1). \end{aligned} \tag{3.17}$$

Since

$$k_{\mathrm{L}}(x_3 - x_{2,\mathrm{II}}) = k_{\mathrm{L}}(x_{2,\mathrm{I}} - x_1), \tag{3.18}$$

the net phase shift for each of the paths due to the light-atom interactions is also zero, provided $\phi_1 = \phi_2 = \phi_3$. At the end of the pulse sequence, the atom is then returned back to the ground state $|g\rangle$.

4 An atom interferometry measurement of the acceleration due to gravity

Now let us consider the phase shift of the interferometer in the presence of gravity. The action along the classical path is now given by

$$\delta\phi = S_{\mathrm{Cl}}/\hbar = \frac{1}{\hbar}\int_{\Gamma} \mathrm{d}t \left[\frac{1}{2}Mv^2 - Mgx\right]. \tag{4.1}$$

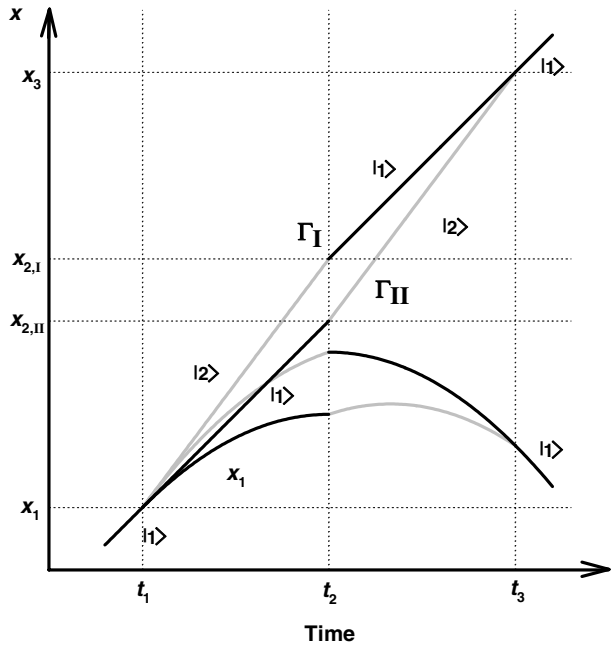

Fig. 2. Phase space diagram of the atom interferometer based on the $\pi/2-\pi-\pi/2$ pulse sequence, showing paths in both absence and presence of gravity. The momentum pulses due to the off-resonant Raman pulses are assumed to be directed upwards. The pulse timing is chosen so that the π pulse is applied near the top of the fountain.

It is a straight forward exercise to show that the evaluation of the action (4.1) for each of the paths is again identical.

There is a non-zero phase difference due to the interaction of the atom with the light. The easiest way to see this is to note that the phase of the optical field only enters into the atomic phase when there is a transition between internal states as given in equations (3.15). Setting $t_2 - t_1 = t_3 - t_2 \equiv \Delta t$, the change in phase shifts relative to (3.18) for each of the two paths is

$$\Delta\phi_{\rm I} = \Delta\phi_{\rm I}|_{\rm no\ gravity} + k_{\rm L}\Delta x|_{\rm I} = +k_{\rm L}\left(\frac{1}{2}g\Delta t^2\right) - (\phi_2 - \phi_1) \qquad (4.2)$$

$$\Delta\phi_{\rm II} = \Delta\phi_{\rm I}|_{\rm no\ gravity} + k_{\rm L}\Delta x|_{\rm II} = +k_{\rm L}\left(2g\Delta t^2 - \frac{1}{2}g\Delta t^2\right) - (\phi_2 - \phi_3)\,, \qquad (4.3)$$

and

$$\Delta\phi \equiv \Delta\phi_{\mathrm{II}} - \Delta\phi_{\mathrm{I}} = k_{\mathrm{L}} g \Delta t^2 + (\phi_1 - \phi_2) - (\phi_2 - \phi_3). \tag{4.4}$$

The origin of the phase shift given by (4.4) is clear from the derivation. An atom at rest will see $\omega_{\mathrm{L}}\Delta t/2\pi$ oscillations of the applied field during the time interval Δt. On the other hand, if the atom moves a distance Δx in the same direction as the light during the same time Δt, it will see $k_{\mathrm{L}}\Delta x/2\pi$ fewer oscillations. The interferometer measurement of g compares the phase shift $k_{\mathrm{L}}\Delta x$ an atom experiences during the first part of the free fall time with the phase shift during the second interval of time. The phase shift can also be interpreted in terms of a Doppler shift where the precision of the measurement given by equation (4.4) increases quadratically in Δt. One power of Δt comes from the fact that $\Delta v \sim g\Delta t$ and the other power comes from the fact that the linewidth of the transition varies inversely as the quantum measurement time, $\Delta t \sim 1/(\Delta\nu_{\mathrm{Ramsey}})$.

This analysis also shows that the interferometric measurement of g is a differential measurement: the phase shift of one part of the atom in the second half of the fall is compared to the phase shift of the other part of the atom in the first half of the fall. Thus, a number of potentially troublesome effects such as the AC Stark shift generated by the optical fields as well as phase shifts due to the rf filters, amplifiers, electro-optic and acousto-optic modulators are greatly suppressed by this pulse sequence.

Note that the phase shift is independent of the quantum scale factor $\hbar/M$. This might lead one to think of the phase shift measured by this atom interferometer as "classical" and different from the "quantum" measurement made by a neutron interferometer. We will now show that both the neutron and atom interferometer measurements of g result from the same basic quantum physics. However, an absolute measurement of g with an atom interferometer has the advantage that the interaction of an atom with a laser field is inherently better understood than the interaction of a neutron with a crystal.

In the neutron interferometer literature, the phase shift is usually calculated by dividing the Lagrangian into two terms $L = L_0 + L_1$, where $L_1(t) = Mgz(t)$ is a small perturbation. (See, for example, Greenberger and Overhauser) [29]. To first order, the action can be calculated as the integral of the perturbative action along the unperturbed path determined by L_0. Evaluation of this integral leads to a net phase shift given by

$$S' \equiv \int_{t_a}^{t_{\mathrm{b}}} L_1 \, \mathrm{d}t \tag{4.5}$$

along the unperturbed path determined by L_0. (In this simplified treatment, we ignore the complications due to the dynamical scattering of neutrons in a

crystal, the multiple interferometer paths taken by the neutrons and possible mass shifts.) A straightforward evaluation of this integral leads to a net phase shift $\Delta\phi = -(Mg/\hbar) \times (\textit{phase space area})$ where the interferometer phase space area is given by $\Delta x \times \Delta t$. The product of $M/\hbar$ and the phase space area are often cited as a measure of the sensitivity of the device.

People who work with neutron interferometers have stressed the significance of a formula where both g and $\hbar$ appear in the same equation. Although this formula explicitly contains g and $\hbar/M$, the area can be written in terms of the momentum transferred by the lattice of wavevector $k_{\mathrm{Latt}} = 2\pi/a$, where a is the interatomic spacing of the lattice plane causing the Bragg scattering. The area is $\Delta x \times \Delta t = (\hbar k_{\mathrm{Latt}}/M)\Delta t \times \Delta t$ so that$\Delta\phi = -k_{\mathrm{Latt}} g \Delta t^2$. Since the neutrons scatter from three portions of the same single crystal of silicon, the relative phases of the three lattice planes $(\phi_1 - \phi_2) - (\phi_2 - \phi_3) = 0$. Thus, this method of calculating the phase shift also gives equation (4.4). Alternatively, the same phase shift can be obtained by the exact calculation where the free evolution is calculated along the true (gravitationally perturbed) path. With this analysis, the $\Delta\phi$ is seen as the phase slip of the neutron with respect to the lattice caused by gravity and is completely analogous to the optical pulse interferometer of Kasevich and Chu [4].

4.1 Circumventing experimental obstacles

The above analysis has been over simplified since we assumed that the frequency of the light is constant. In practice, this type of interferometer has been used in an atomic fountain of cold atoms with free fall times up to 2×0.16 seconds, corresponding to a Doppler shift $k_{\mathrm{L}} g t^2$ of several Megahertz. Unless the frequency of the light is changed, atoms that are in resonance with the first laser pulse will be far out of resonance with the remaining pulses. Also, during this time, the states $|1\rangle$ and $|2\rangle$ must be stable against radiative decay. Also, if the frequency of the optical field is not stable during the drift time of the interferometer, the fringes will wash out. Since the measurement time is so long, a change in the optical frequency of a few Hertz will cause the interferometer to cycle through 2π radians. Currently, lasers with this frequency stability do not exist.

Both of these requirements are satisfied if we use stimulated transitions between two (magnetic field insensitive) ground states of the atom separated by a hyperfine splitting. If the two laser beams k_1 and k_2 are counter propagating, the phase shift seen by the atom is given by $(k_1 + k_2) \times \Delta x$, approximately twice the shift relative to a single beam. On the other hand, only the frequency difference of the two beams is critical for the measurement. While it is difficult to control the absolute frequency of light, it is relatively easy to phase lock two laser beams relative to each other, either by generating the second frequency with an electro-optic or acousto-optic

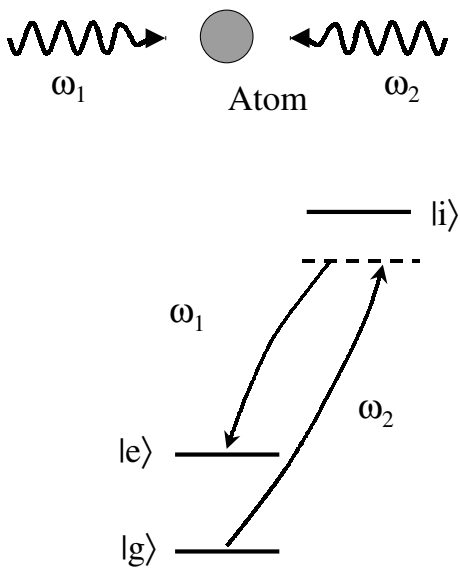

Fig. 3. An atom undergoes a stimulated Raman transition. It absorbs a photon of frequency ω_2 and emits another one (via a stimulated emission) of frequency ω_1. Since both photons carry momentum, and because momentum has to be conserved in the process, the atom receives a recoil momentum kick.

device or by phase locking two independent lasers to a stable microwave reference. Thus, by inducing a two-photon transition with counter propagating beams, the extraordinary requirement of sub-Hertz optical stability is reduced to the much more modest demand of sub-Hertz microwave stability. This measurement of the acceleration due to gravity converts the measurement of an optical phase change into a microwave measurement relative to a stable microwave reference. The introduction of Raman transitions to induce velocity changes is the closest thing to a free lunch that this physicist has ever encountered.

4.2 Stimulated Raman transitions

In this section, we introduce some of the formalism needed to analyze the atom interferometer phase shifts using Raman transitions. Consider the three-level atom in Figure 3 consisting of two ground-state hyperfine levels $|g\rangle$ and $|e\rangle$ with rf splitting ω_{eg} coupled by optical transitions to an intermediate state $|i\rangle$. Assume the atom is initially prepared in state $|g\rangle$. Two counter propagating beams of frequency ω_1 and ω_2 induce stimulated Raman transitions to level $|e\rangle$ if $\omega_1 - \omega_2 - \Delta\omega_{\mathrm{D}} \simeq \omega_{eg}$, where

$\Delta\omega_{\rm D} = (\mathbf{k}_1 - \mathbf{k}_2)\cdot\mathbf{v}$. When the beams counter propagate, $\Delta\omega_{\rm D} \simeq 2\mathbf{k}_1\cdot\mathbf{v}$, so the transition has a Doppler sensitivity twice that of a single-photon optical transition. For Cs, the two-photon Raman transition has a Doppler sensitivity of 23.5 kHz/(cm/s) when the Raman beams are nearly resonant with the 852 nm optical transition.

We present a brief summary of the theory underlying the two-photon, velocity-sensitive Raman transition. The essential results are: (1) in certain regimes the three-level system can be viewed as a two-level system coupled with an effective Rabi frequency given by the two-photon transition rate; (2) the internal state of the atom is correlated with its momentum; and (3) the two-photon Raman excitation can be modeled by a traveling-wave excitation of frequency $\omega_1 - \omega_2 \simeq \omega_{eg}$ and effective propagation vector $\mathbf{k}_{\rm eff} \equiv \mathbf{k}_1 - \mathbf{k}_2 \simeq 2\mathbf{k}_1$ for counter propagating beams.

The key assumption in the treatment which follows is that the detuning of the frequencies ω_1 and ω_2 from the optical resonance is large enough that spontaneous emission from the intermediate level $|i\rangle$ can be neglected. When the detuning from the intermediate level is large, the intermediate level can be adiabatically eliminated from the interaction picture Schrödinger equations and the dynamics of the three-level system reduce to those of a two-level system.

The Hamiltonian for the three-level system is

$$\hat{H} = \frac{\hat{\mathbf{p}}^2}{2m} + \hbar\omega_e|e\rangle\langle e| + \hbar\omega_i|i\rangle\langle i| + \hbar\omega_g|g\rangle\langle g| - \mathbf{d}\cdot\mathbf{E}. \tag{4.6}$$

In this case the driving electric field contains two frequency components:

$$\mathbf{E} = \mathbf{E}_1\cos(\mathbf{k}_1\cdot\mathbf{x} - \omega_1 t + \phi_1) + \mathbf{E}_2\cos(\mathbf{k}_2\cdot\mathbf{x} - \omega_2 t + \phi_2). \tag{4.7}$$

The frequencies $\omega_1 \simeq \omega_i - \omega_g$ and $\omega_2 \simeq \omega_i - \omega_e$ while the difference frequency $\omega_1 - \omega_2 \simeq \omega_{eg}$. For counter propagating beams $\mathbf{k}_1 \simeq -\mathbf{k}_2$. We have explicitly neglected spontaneous emission from the off-resonant excitation of the optical transition.

Following the procedure given in Section 2.5 while using the interaction coefficients from equation (2.51) along with an additional coefficient for the corresponding intermediate state $|i, \mathbf{p} + \hbar\mathbf{k}_1\rangle$, one obtains a set of coupled first-order differential equations for $c_{g,\mathbf{p}}$, $c_{i,\mathbf{p}+\hbar\mathbf{k}_1}$, and $c_{e,\mathbf{p}+\hbar\mathbf{k}_{\rm eff}}$. In the limit where the detunings $\omega_1 - (\omega_i - \omega_g)$ and $\omega_2 - (\omega_i - \omega_e)$ are much larger than the Rabi frequencies, the coefficients $c(t)$ vary slowly compared to the explicitly time-dependent terms. Thus, we can adiabatically eliminate all coefficients for the intermediate states. We are then left with coupled equations for a two-level system in an external driving field. In the spinor representation for $|e, \mathbf{p} + \hbar\mathbf{k}_{\rm eff}\rangle$ and $|g, \mathbf{p}\rangle$, the Hamiltonian describing this

time evolution is

$$\hat{H} = \frac{\hbar}{2}\begin{bmatrix} \Omega_e^{\mathrm{AC}} & (\Omega_{\mathrm{eff}})\mathrm{e}^{-i(\delta_{12}t+\phi_{\mathrm{eff}})} \\ (\Omega_{\mathrm{eff}})\mathrm{e}^{i(\delta_{12}t+\phi_{\mathrm{eff}})} & \Omega_g^{\mathrm{AC}} \end{bmatrix}, \tag{4.8}$$

where we define

$$\Omega_e^{\mathrm{AC}} \equiv \frac{|\Omega_e|^2}{2\Delta},\ \Omega_g^{\mathrm{AC}} \equiv \frac{|\Omega_g|^2}{2\Delta}, \tag{4.9}$$

$$\delta_{12} \equiv (\omega_1 - \omega_2) - \left(\omega_{eg} + \frac{\mathbf{p}\cdot\mathbf{k}_{\mathrm{eff}}}{m} + \frac{\hbar|\mathbf{k}_{\mathrm{eff}}|^2}{2m}\right), \tag{4.10}$$

$$\Omega_e \equiv -\frac{\langle i|\mathbf{d}\cdot\mathbf{E}_2|e\rangle}{\hbar},\ \Omega_g \equiv -\frac{\langle i|\mathbf{d}\cdot\mathbf{E}_1|g\rangle}{\hbar}, \tag{4.11}$$

$$\Omega_{\mathrm{eff}}\mathrm{e}^{-i\phi_{\mathrm{eff}}} \equiv \frac{\Omega_e^*\Omega_g}{2\Delta}\mathrm{e}^{i(\phi_1-\phi_2)}, \tag{4.12}$$

with the real angle ϕ_{eff} chosen to make Ω_{eff} a positive real number.

Here $\Delta \simeq \omega_1 - (\omega_i - \omega_g)$ is the detuning from the optical resonance as illustrated in Figure 4. As expected, momentum recoil explicitly shows up in the one-to-one correlation between the atom's internal state and its momentum for the two states $|e, \mathbf{p}+\hbar\mathbf{k}_{\mathrm{eff}}\rangle$ and $|g, \mathbf{p}\rangle$ coupled by this Hamiltonian, and the dynamics are governed by the difference frequency $\omega_1 - \omega_2$. The effective detuning δ_{12} from the Raman resonance contains the expected Doppler-shift and recoil-shift terms. The main diagonal elements of the Hamiltonian are the AC Stark shifts of levels $|e\rangle$ and $|g\rangle$. The relative shift of the two levels caused by AC Stark shifts is

$$\delta^{\mathrm{AC}} \equiv \left(\Omega_e^{\mathrm{AC}} - \Omega_g^{\mathrm{AC}}\right). \tag{4.13}$$

For simplicity we have neglected contributions to the AC Stark shift from the couplings shown in Figure 4 by the dotted lines. These additional terms can be found in Weiss *et al.* [15].

This Hamiltonian is similar in form to equation (2.9) for a two-level atom except for the AC Stark shift terms on the main diagonal. Given one additional step, it is possible to transform it into a time-independent Hamiltonian of the exact form of $\hat{H}_{\mathrm{R}}$ in equation (2.50) so that the solution for a two-level atom can be directly applied. This extra step is to first make a uniform shift of the energy scale by $-\hbar(\Omega_e^{\mathrm{AC}} + \Omega_g^{\mathrm{AC}})/2$. This anti symmetrizes the main diagonal elements to $\pm\hbar\delta^{\mathrm{AC}}/2$, which can be combined with the $\mp\hbar\delta_{12}/2$ terms that arise in the transformation to the rotating frame. For further details, the reader is referred to Young *et al.* [8].

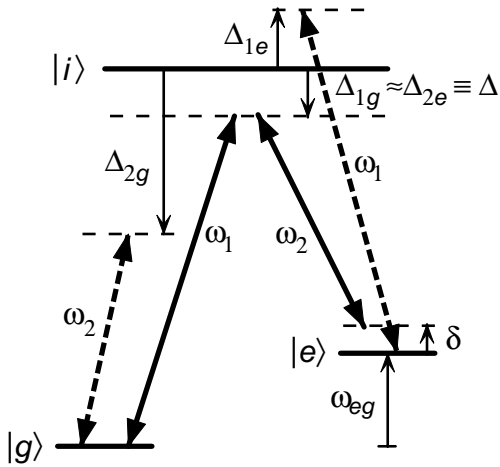

Fig. 4. Schematic representation for a three-level atom. Two light fields at frequencies ω_1 and ω_2 couple states $|g\rangle$ and $|e\rangle$ *via* the intermediate state $|i\rangle$. The one- and two-photon detunings are Δ and δ, respectively. Additional AC Stark shifts are caused by the interaction of ω_1 and ω_2 with the wrong levels, as indicated by the dashed arrows.

4.3 Frequency sweep and stability issues

Typical free-fall times of an atomic fountain-based atom interferometer is 0.3 seconds. The corresponding velocity change $g\Delta t = 300$ cm/s give a Doppler shift of ~ 4 MHz. Since the linewidth of the transition $\sim 1/\Omega_{\text{eff}} \sim 20$ kHz, the laser frequency $\omega_1 - \omega_2$ of the Raman pulses must be changed in a phase stable manner in order to keep in resonance with the atoms. At the time of our initial experiment, inexpensive rf oscillators did not remain phase locked when the frequency was swept.

Our initial solution [4] was to use three inexpensive digital frequency synthesizers (Stanford Research Systems) running at fixed frequencies ω_1, ω_2 and ω_3 driven by the same master clock signal derived from a Loran-C receiver. An rf switch mixes each of the frequencies with a phase stable high frequency oscillator at 1.77 GHz that then drives an electro-optic modulator. Laser light at frequency ω_{L} passing through the modulator has rf sidebands at ω_{rf} added to the carrier frequency ω_{L}. An acousto-optic modulator is used to switch the light onto the atoms at the appropriate time. Note that the Ramsey method is insensitive to the slight amount of timing jitter that may occur in the AO modulator. For the cesium experiment, we used two independent diode lasers that were phased locked to an rf signal constructed by mixing a phase stable 9.2 GHz oscillator with a low frequency digital sweep oscillator. The details of how the feedback loop locked to the correct

frequency were not important as long as the lock was established before the light was turned onto the atoms.

4.4 Vibration isolation

The phase shift measurements described above require control of the optical frequencies to a small fraction of one optical cycle during the free-fall time. Vibrations in the laboratory do not affect the motion of the falling atoms, but vibrations of the Raman beam mirrors can perturb the phase of the light field in the interaction region. We have employed two methods for insuring sufficient phase stability of the light field incident on the atoms.

The simplest technique for obtaining phase-stable light fields applies when the two Raman beams at frequencies ω_1 and ω_2 can be allowed to copropagate through all of the same optics until they pass through the interaction region. Since $\mathbf{k}_1$ and $\mathbf{k}_2$ only differ at the $\sim 10^{-5}$ level, the Doppler shifts from vibrations of these mirrors are nearly identical for the two beams, so they cancel with high accuracy in the Raman frequency difference. All of the experiments described in the previous section use velocity-sensitive transitions, which require counter propagating beams. Consequently, a final mirror is used after the interaction region to retro reflect both beams back through the interaction region. If the atoms are moving at a nonzero velocity along the direction of $\mathbf{k}_{\text{eff}}$, then the Doppler shift of the two-photon detuning can be used to select which pair of velocity-sensitive beams drives the transition. Thus, the problem of obtaining stable phase-fronts reduces to vibrationally isolating the final retro-reflection mirror and the motion of an atom is measured relative to the retro-reflecting mirror.

An active vibration isolation system is used to stabilize this mirror. A sensitive, low frequency accelerometer rigidly connected to the reference mirror measures the acceleration of the mirror/accelerometer assembly suspended passively by springs. The acceleration signal is processed through a digital feedback loop to produce a signal to a transducer that reduces the amplitude of the accelerations. The reduction of the accelerometer error signal with the feedback loop closed is reduced by up to a factor of 200 in the frequency range from $\sim 0.01 - 100$ Hz. To actually achieve this level of isolation along $\mathbf{k}_{\text{eff}}$ requires a ~ 1 mrad alignment of the sensor axis to $\mathbf{k}_{\text{eff}}$, and a similarly good alignment of the atomic trajectory below the sensor to avoid problems due to tilt [30].

Although mechanically and electronically easier to implement, the retro-reflection approach has the drawback that extra beams are present in the interaction region. These beams may introduce spurious phase shifts in the atomic coherence due to, for example, the AC Stark effect or mechanical effects from standing-wave potentials. Furthermore, this approach is completely unacceptable when using adiabatic transfer instead of stimulated Raman transitions. In that case, the Doppler shift of the atoms can be

large enough to detune the two-photon resonance for the undesired beam pair, but not the single-photon resonance, so the atoms will incoherently scatter photons from those beams. Consequently, for interferometers using adiabatic transfer, or those using stimulated Raman transitions either near zero velocity or for which the undesired light shifts are unacceptable, ω_1 and ω_2 must be independently directed to the interaction region.

Since the photon recoil measurement uses an atom interferometer based on adiabatic passage, ω_1 and ω_2 must reflect off of several mirrors that are not shared by the two beams, so there is no common-mode cancelation of vibrations. Rather than trying to vibrationally isolate all of these mirrors, we built a stable reference platform suspended immediately above the vacuum chamber on which we measure the beat note of the two Raman laser beams. The Raman frequency difference is then locked to a stable rf source. Since the phase of the light must be stable from the instant that it is pulsed on, it is not sufficient to measure the vibrations by detecting the beatnote between the Raman beams. Instead, we overlap with the Raman beams a cw tracer beam detuned 8 nm from the atomic resonance.

The observed improvement of the g measurement signal-to-noise with active vibration isolation matches to within a factor of two the optimum performance expected from the reduction of the accelerometer error signal. The effect of vibration isolation on fringe contrast has been observed for the photon recoil measurement that is described below. Without vibration corrections, the fringe contrast falls 50% as T is increased to about 1 ms. When vibrations are canceled using the tracer beams, with the active platform isolation disabled, the contrast drops 50% by $T \approx 30$ ms. With the active isolation enabled, the contrast is still over 60% of its initial value at $T = 150$ ms.

4.5 Experimental results

Each cycle of the experiment begins by capturing cesium atoms in a magneto-optical trap in a low density vapor cell. After ∼0.6 seconds, the atoms are further cooled in polarization gradient molasses by shifting the frequencies of the molasses beams from a detuning of 20 MHz to 60 MHz, and then launched upwards by shifting the relative frequencies of the molasses beams. In the final stages of the launch, the light intensity is ramped down in 300 μs so that the atoms can be adiabatically cooled to still colder temperatures ($1.3 - 1.5$ μK). Since our experiment is not shot noise limited, atoms in the $|F = 3, m_{\rm F} = 0\rangle$ state within a narrow slice of the initial velocity distribution are selected through a series of stimulated microwave and optical pulses in order to increase the interferometer contrast. Stimulated Raman pulses generated by two phase-locked diode lasers are used to produce the interferometer pulses when the atoms are inside a quadruple magnetic shielded region with a bias field of 2 mG. The population of atoms

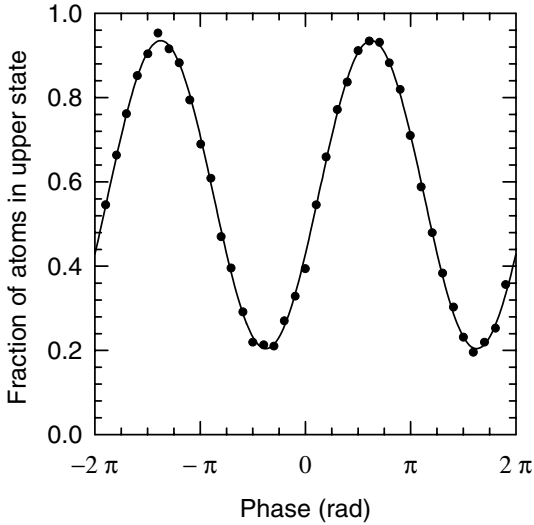

Fig. 5. Typical Doppler sensitive interferometer fringe for $T = 160$ ms. The data shown was taken in one minute and a least squares fit determines the local gravity to an uncertainty of 3×10^{-9} g.

in the $|4, 0\rangle$ state is measured for each launch by recording the fluorescence from the atoms illuminated by circularly polarized light tuned to $F = 4$ ground state to $F' = 5$ excited state transition. Next, the remaining atoms in the $F = 3$ state are transferred to the $F = 4$ state and the fluorescence measurement is repeated in order to measure the total number of atoms that have made it to the detection region.

Figure 5 shows the interferometer fringes for an interferometer time $2T$ of 0.32 seconds. Each data point represents a single launch of atoms. We emphasize the equivalent of 5.9×10^5 cycles of phase have accumulated during the measurement time. The short term stability of the interferometer is $\Delta g/g \sim 3 \times 10^{-9}$ after one minute of data taking. Figure 6 shows the results of over 2 days of continuous data taken with our atom interferometer. The data is plotted with a tidal model that includes only the elastic deformation of the earth and another model that also adds ocean loading effects. Figure 7 shows the difference between the data and the two tidal models. Each data point corresponds to an integration time of 1 minute. The statistical uncertainty for this data is $\Delta g/g \leq 1 \times 10^{-10}$. The long term stability of this interferometer has been demonstrated out to $\sim 10^4$ seconds.

During the course of our experiment we ran a Micro-g Solutions FG5 absolute gravimeter for three days to measure the absolute value of g. This instrument is a Michelson optical interferometer with one arm defined by a

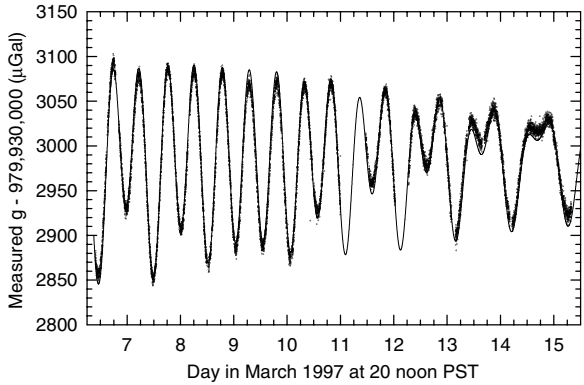

Fig. 6. Gravity data taken over a period of 9 days. The data points correspond to approximately one minute of integration time shown in Figure 5. The solid line is a single parameter fit using a theoretical model of the gravity tides at our measurement site, Stanford, California.

freely falling corner-cube and has a quoted relative uncertainty of 2 parts per billion (ppb). A comparison with the value of g we obtained in a 2-day run shows a difference of (7 ± 7) ppb. This comparison was limited mostly by a 5 ppb uncertainty in our measurement of the local gravity gradient which produces a 3 ppb correction per cm vertical displacement. Direct comparison of the noise of both instruments also showed that our atom interferometer has 4 times higher resolution than the falling corner cube gravimeter.

Table 1 shows the most important identified systematic effects and their associated uncertainties. Other effects, such as magnetic field gradients, wavefront curvature, speckle, dispersion in the air and windows, timing and switching errors in the optical pulses, etc., were experimentally found to be below the 0.1 ppb level and are not listed. We have also estimated relativistic corrections (< 0.1 ppb) and the effect of a changing effective wavevector due to different propagation delays during the interferometer sequence (corrected to an uncertainty of < 0.1 ppb). A summary of the systematic effects can be found in [31].

We have varied the time of the $\pi/2 - \pi - \pi/2$ pulses relative to the time of the launch. We observe a variation in g that quantitatively agrees with a calculated change due to the gravity gradient and the change in the magnitude of the k-vectors of the light. The fit of our data to the calculated curve (residual $\ll 1$ ppb) allows us to set an upper limit to a systematic effect due to any "trajectory effect". This test also states that the presence of both Raman frequencies ω_1 and ω_2 in the downward and upward traveling beams, which could excite off-resonant coherences that would affect the measured

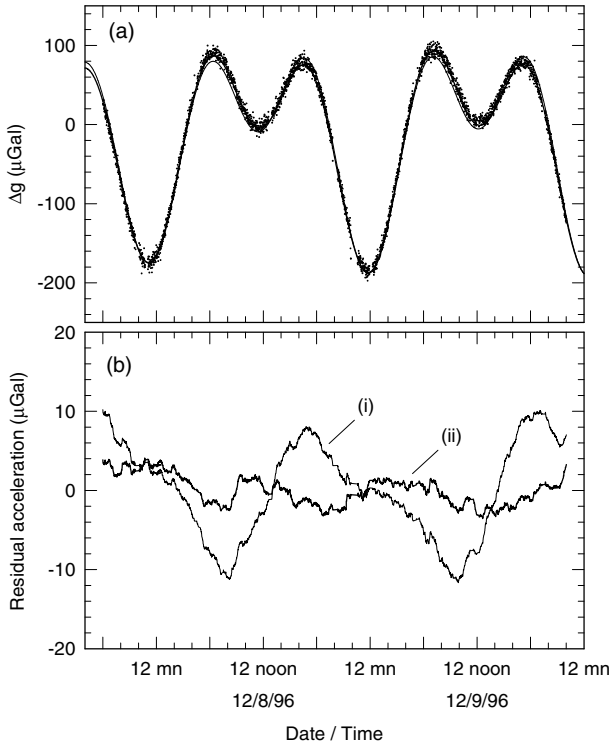

Fig. 7. (a) A measurement of g taken over another two day period. Here we plot two tidal models. (b) The residuals of the data with respect to a tidal model where (i) the Earth is modeled as a solid elastic object, and (ii) where the effects of ocean loading of the Earth is taken into account.

phase shift, is not a significant problem. This potential problem becomes especially acute when the π-pulse is applied when the atoms are near the apogee of their trajectory and would appear as an unaccounted phase shift as the trajectory is varied.

At ppb levels, uncertainties due to environmental effects become significant. The major uncertainties are listed in Table 1. However, these effects are not part of the instrumental uncertainty. The measurement presented here is a million-fold increase in absolute accuracy obtained by atom interferometers. From our study of the systematic effects of this measurement, we feel that further improvements in the control of Coriolis effect, *e.g.*, by rotating the whole system, and ensuring that there is no synchronized noise on the vibration isolator, should lead to a relative uncertainty on the order of one part in 10^{10}.

Table 1. Major known potential systematic effects. Major sources of potential systematic effects are tabulated. Systematic effects that are 0.1 ppb or less are not listed including timing, switching and chirping of pulses, Zeeman and DC Stark shifts, dispersion of light in air, Cs vapor and windows, tilt of Raman beam with respect to the vertical, standing waves effect, leakage light, wavefront curvature and speckle, Berry phase, second order Doppler shift, gravitational redshift and other relativistic effects. Environmental effects, while not part of our instrumental uncertainty, are important for comparing g measured at different times. Other environmental effects include water table correction.

Systematic Error	Uncertainty (ppb)
Instrumental	
RF phase shift	2
Coriolis Effect	2
ac Stark shift	1
Synchronous noise	1
Dependence on pulse timing	1
Retro reflection	0.6
Laser lock offset	0.4
Cs Wavelength	0.3
Gravity gradient	0.2
Cold collision	0.2
Synchronous vibration	0.2
Synchronous fields	0.2
Changing k-vector	0.1
Overall instrumental uncertainty	**3.4**
Environment	
Pressure correction	1
Ocean loading	1
Other environmental effects	2

5 Interferometry based on adiabatic transfer

The first atom interferometers were constructed using stimulated Raman transitions, which have the many advantages discussed above. Disadvantages of this technique in precision measurements include its sensitivity to spatial inhomogeneity of the laser beams and laser intensity fluctuations, and the systematic errors that can arise from ac Stark shifts. Also, several atom interferometer experiments have sensitivities that can be greatly enhanced by applying multiple light pulses to deliver a large number of photon recoils, but adding more pulses also increases the sensitivity of the interferometer to intensity variations. For a laser beam with a Gaussian

intensity profile, different atoms will sample different intensities so that the π pulse condition cannot be simultaneously met for atoms at all locations in the beam. Increasing the laser beam waist reduces this problem, but also decreases the Rabi frequency (for fixed laser power), which reduces the atom signal size for typical experimental parameters. In the first version of the photon recoil experiment, spatial variation of the beam intensity limited the π pulse transfer efficiency to 85%.

Fluctuations of the beam intensities also cause deviations from the desired π pulse condition. This effect is second order in the fractional intensity noise, but if several pulses are applied, it can still become a significant noise source unless the laser intensities are actively controlled. The most pernicious effects of intensity fluctuations, however, involve ac Stark shifts. With stimulated Raman transitions, ac Stark shifts can make sizable contributions to the atom interferometer phase. Typically, the ac Stark shift of the two-photon transition Ω^{AC} is of the same size as the effective Rabi frequency Ω_{eff}. Consequently, for a single π pulse, the ac Stark shift can cause a phase shift that is a sizable fraction of a complete cycle. The average Stark shift can generally be zeroed by properly adjusting the ratio of beam intensities, but the phase shift remains linearly sensitive to intensity variations and inhomogeneities around the set values. For example, a major source of systematic error in the first photon recoil measurement made by the Stanford group [15] was the ac Stark shift caused by standing waves. The average ac Stark shift had been zeroed in this experiment, but the presence of standing waves caused a strong modulation of the ac Stark shift along the direction of the beam, which caused a systematic shift of the interferometer phase.

An alternate technique for changing the states of atoms and molecules is adiabatic passage, which was first used in magnetic spin resonance [85]. In our current photon recoil experiment, we use an adiabatic passage technique first introduced by Gaubatz *et al.* [32]. In this form of adiabatic passage, time-delayed, on-resonant light fields efficiently transfer atoms between two states. The atoms adiabatically follow an eigenstate of the atom-field interaction Hamiltonian that is never coupled to the excited state. This method yields two important benefits: (1) despite the use of on-resonant light, spontaneous emission can be nearly completely avoided, and (2) the atoms experience very low ac Stark shifts [40]. Population transfer with adiabatic passage was first demonstrated in the optical regime by passing a molecular beam through two displaced Gaussian beams [32]. The possibility of using counterpropagating beams to obtain momentum transfer for use in atom interferometry was quickly pointed out by Marte *et al.* (1991) [34] and by Bordé (1992) [60]. Momentum transfer *via* adiabatic passage was quickly demonstrated by Pillet *et al.* (1993) [36], Lawall and Prentiss (1994) [37], and Goldner *et al.* (1994) [35]. More recently, we have demonstrated

an atom interferometer using adiabatic passage to split, redirect, and recombine the atomic wave packets [39].

5.1 Theory of adiabatic passage with time-delayed pulses

Consider the three-level atom of Figure 4 interacting with counterpropagating laser beams of frequencies ω_1 and ω_2. For adiabatic passage the single-photon detuning is generally set near zero, so the relaxation rate Γ of the intermediate state $|i\rangle$ cannot be neglected. Its effect can be included by adding to the Hamiltonian of equation (4.6) a non-Hermitian term, as in Oreg *et al.* [38]. The total Hamiltonian is then

$$\hat{H} = \frac{\hat{\mathbf{p}}^2}{2m} + \hbar\omega_e|e\rangle\langle e| + \hbar\left(\omega_i - i\Gamma/2\right)|i\rangle\langle i| + \hbar\omega_g|g\rangle\langle g| - \mathbf{d}\cdot\mathbf{E}, \tag{5.1}$$

where the electric field is given by equation (4.7). We will neglect here the off-resonant couplings of $|e\rangle$ and $|i\rangle$ by ω_1, and $|g\rangle$ and $|i\rangle$ by ω_2, as shown by the dashed lines in Figure 4. (In a real experiment, these couplings are important since they can limit the transfer efficiency and can be the dominant source of ac Stark shifts. The numerical simulations by Weitz *et al.* include these couplings [39]).

We again use the interaction picture. For adiabatic passage, we cannot adiabatically eliminate the population of the excited state as with the off-resonant Raman case, so the interaction state vector has the form

$$|\psi\rangle = \begin{pmatrix} c_{e,\mathbf{p}+\hbar\mathbf{k}_{\rm eff}}(t) \\ c_{i,\mathbf{p}+\hbar\mathbf{k}_1}(t) \\ c_{g,\mathbf{p}}(t) \end{pmatrix}, \tag{5.2}$$

where $\mathbf{k}_{\rm eff}$ is the effective wave vector for the two-photon transition. The interaction Hamiltonian is

$$\hat{H}_{\rm int} = \frac{\hbar}{2}\begin{pmatrix} 0 & \Omega_e^* e^{i(\Delta_2 t-\phi_2)} & 0 \\ \Omega_e e^{-i(\Delta_2 t-\phi_2)} & -i\Gamma & \Omega_g e^{-i(\Delta_1 t-\phi_1)} \\ 0 & \Omega_g^* e^{i(\Delta_1 t-\phi_1)} & 0 \end{pmatrix}, \tag{5.3}$$

where the single-photon detunings of ω_1 and ω_2 are

$$\begin{aligned} \Delta_1 &= \omega_1 - (\omega_i - \omega_g) + \frac{|\mathbf{p}|^2 - |\mathbf{p}+\hbar\mathbf{k}_1|^2}{2m\hbar}, \\ \Delta_2 &= \omega_2 - (\omega_i - \omega_e) + \frac{|\mathbf{p}+\hbar\mathbf{k}_{\rm eff}|^2 - |\mathbf{p}+\hbar\mathbf{k}_1|^2}{2m\hbar}, \end{aligned} \tag{5.4}$$

the Rabi frequencies Ω_e and Ω_g are given by equations (4.11), and the two-photon detuning $\delta_{12} = \Delta_1 - \Delta_2$ agrees with the definition given in

equation (4.10). In the zero-detuning case $\Delta_1 = \Delta_2 = 0$, the Hamiltonian of equation (5.3) simplifies to

$$\hat{H}_{\rm int} = \frac{\hbar}{2} \begin{pmatrix} 0 & \Omega_e^* \mathrm{e}^{-i\phi_2} & 0 \\ \Omega_e \mathrm{e}^{i\phi_2} & -i\Gamma & \Omega_g \mathrm{e}^{i\phi_1} \\ 0 & \Omega_g^* \mathrm{e}^{-i\phi_1} & 0 \end{pmatrix}. \tag{5.5}$$

Then for any Ω_e and Ω_g, there exists an eigenvector of $\hat{H}_{\rm int}$ with eigenvalue zero, given by

$$|\Psi_{\rm D}\rangle = \begin{pmatrix} \sin\theta \mathrm{e}^{-i\phi} \\ 0 \\ \cos\theta \end{pmatrix}, \tag{5.6}$$

where the real angles θ and ϕ are defined by the relation

$$\tan\theta \mathrm{e}^{-i\phi} = -\frac{\Omega_g}{\Omega_e} \mathrm{e}^{i(\phi_1 - \phi_2)}. \tag{5.7}$$

This eigenvector has two amplitudes for excitation from the two lower levels to the excited state that cancel. Consequently, despite the presence of on-resonance light, an atom in $|\Psi_{\rm D}\rangle$ will not experience spontaneous emission. This state is consequently referred to as the non coupled, or "dark" state. Since the single-photon detuning is zero, the ac Stark shift for a three-level system is zero even if the transfer is not completely adiabatic [40]. The presence of additional energy levels introduces an ac Stark shift, but if the detuning of these states is sufficient, the ac Stark shift can still contribute much less than one cycle of phase shift to an interferometer during the time of the light pulse. Numerical calculations of transfer efficiencies and ac Stark shifts for realistic experimental parameters have been performed by integrating the time-dependent Schrödinger equation showing that adiabatic transfer using the cesium $\mathrm{P}_{1/2}$ excited state is superior to stimulated Raman transitions for both transfer efficiency and ac Stark shifts [40].

If $\Omega_e = \Omega_e(t)$ and $\Omega_g = \Omega_g(t)$, but the variation with time is sufficiently slow that the system can evolve adiabatically, then the steady-state solution of equation (5.6) still applies [41]. To characterize the requirements for adiabaticity, we define an effective Rabi frequency

$$\Omega_0 = \sqrt{\Omega_e^2 + \Omega_g^2}. \tag{5.8}$$

If an atom is in the dark state defined by the light fields at one time, and the dark-state parameters θ and ϕ are varied gradually over a time $\tau \gg 1/\Omega_0$ for $\Omega_0 \gg \Gamma$, or $\tau \gg \Gamma/\Omega_0^2$ for $\Omega_0 \ll \Gamma$, then the atom will follow along in the dark state defined by the light, without undergoing excitation into $|i\rangle$. Note that this adiabaticity criterion does not preclude turning on a single

beam instantaneously, nor suddenly turning both beams on or off together, since none of these operations forces a rapid change of θ or ϕ. On the other hand, if both beams are turned on or off together, care must be taken so that the ratio of two Rabi frequencies in equation (5.6) is maintained.

The population transfer achieved with adiabatic passage is qualitatively very different from the transfer achieved with stimulated Raman transitions. For stimulated Raman transitions, the atomic state vector evolves coherently regardless of the initial state of the system when the light pulse is applied. Consequently, light pulses that take an atom from $|g\rangle$ to $|e\rangle$ will also take an atom from $|e\rangle$ to $|g\rangle$. The effects of adiabatic transfer pulses, however, depend strongly on the initial state of the system. For example, if an atom starts out in $|g\rangle$, then Ω_e must be turned on alone at the beginning of the adiabatic pulse sequence in order to avoid spontaneous emission. If Ω_e alone were applied to an atom initially in $|e\rangle$, then the atom would scatter photons, eventually resulting in an incoherent transfer into $|g\rangle$ *via* optical pumping.

More generally, suppose the state of the atom at time $t = 0^-$ is $|\psi(0^-)\rangle$, and that the laser beams are turned on at time $t = 0$ with phases and intensities defining a dark state $|\Psi_{\rm D}(0^+)\rangle$. The projection $|\Psi_{\rm D}(0^+)\rangle\langle\Psi_{\rm D}(0^+)|\psi(0^-)\rangle$ of the initial atomic state onto the dark state gives the fraction of the initial state that will not scatter photons, and will adiabatically follow the dark state as it slowly changes to $|\Psi_{\rm D}(t)\rangle$. Assuming that the beam intensities are varied sufficiently slowly that the transfer is completely adiabatic, the coherently transferred part of the wave function immediately after the end of an adiabatic transfer pulse of duration τ is

$$|\psi(\tau^+)\rangle = |\Psi_{\rm D}(\tau^-)\rangle\langle\Psi_{\rm D}(0^+)|\psi(0^-)\rangle \cdot \tag{5.9}$$

5.2 Atom interferometry using adiabatic transfer

We now have the tools to construct an atom interferometer based on adiabatic transfer. Figure 8 shows the pulse sequences that, along with their complements formed by interchanging Ω_e and Ω_g, are the basis for constructing atom interferometers using adiabatic passage. The dark state at any time during the sequences is determined by substituting the laser phases and Rabi frequencies into equations (5.6) and (5.7). The net effect of each of these sequences can be determined from equation (5.9), using the dark states $|\Psi_{\rm D}(0^+)\rangle$ and $|\Psi_{\rm D}(\tau^-)\rangle$ corresponding to the beam phases and intensities at the beginning and end of the pulse sequence, respectively. In Figure 8a, the initial and final dark states are $|\Psi_{\rm D}(0^+)\rangle = |g\rangle$ and $|\Psi_{\rm D}(\tau^-)\rangle = |e\rangle$, so an atom initially in $|g\rangle$ is completely transferred to $|e\rangle$. Reversing the roles of Ω_e and Ω_g provides for the opposite transfer. In Figure 8b, the initial dark state is still $|g\rangle$, but the final dark state is $(|g\rangle + |e\rangle)/\sqrt{2}$, so this sequence transfers an atom in $|g\rangle$ into an equal coherent superposition

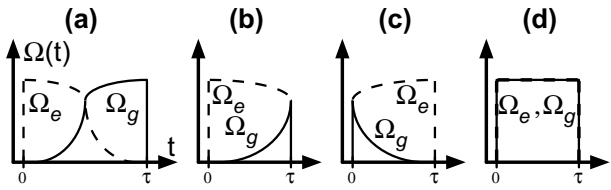

Fig. 8. Pulse shapes used to construct an atom interferometer using adiabatic transfer. Changing the field amplitudes Ω_g and Ω_e with time (a) transfers an atom from $|g\rangle$ to $|e\rangle$, (b) transfers an atom from $|g\rangle$ to $(|g\rangle + |e\rangle)/\sqrt{2}$, (c) transfers an atom from $(|g\rangle + |e\rangle)/\sqrt{2}$ to $|g\rangle$, and (d) projects an atom onto $(|g\rangle + |e\rangle)/\sqrt{2}$, and then leaves it off in that state.

of $|g\rangle$ and $|e\rangle$. A pulse of this type splits a single path into two paths for an atom interferometer. Figure 8c is the time reversal of Figure 8b, so it projects the initial state of the atom onto the equal coherent superposition with phase defined by $|\Psi_{\rm D}(0^+)\rangle$, and then transfers that fraction of the wave function into $|g\rangle$. This sequence combines or redirects paths in an atom interferometer. Similarly, Figure 8d projects the initial state onto the superposition state defined by $|\Psi_{\rm D}(0^+)\rangle$, but then leaves the atom still in that superposition state. This pulse sequence is used to split interferometer paths when the atom must start and remain in a superposition state.

The pulse sequences of Figures 8a-d require tailored pulse shapes. These shapes were produced by independently controlling beam intensities using acousto-optic modulators. Figure 9 shows a standard Ramsey-Bordé interferometer and its implementation using the adiabatic transfer pulses from Figure 8 [39]. The first pulse splits the initial state into a coherent superposition of $|g\rangle$ and $|e\rangle$. After the atom is allowed to freely evolve for a time T, a second pulse is applied that projects the atomic wave function onto the dark superposition state $|\Psi_{\rm D}(t_2^+)\rangle$, where t_2 is the start time of the second pulse, as shown in Figure 9b. Then Ω_g is turned off so that the atom is left in $|g\rangle$. (Turning off Ω_e instead also leads to a valid interferometer, which is the upper interferometer of Fig. 1b for the photon recoil measurement.) The fraction of the wave packet that is out of phase with $|\Psi_{\rm D}\rangle$ will undergo spontaneous emission, and thus lose coherence. It may contribute to the background signal of the interferometer, but will not cause a systematic shift of the fringes. The third pulse splits each of the two paths in state $|g\rangle$ into superposition states. After waiting again for a time T, two of the paths overlap spatially. A final pulse applied at this time projects the wave function onto the superposition state $|\Psi_{\rm D}(t_4^+)\rangle$, again evaluated at the start of the pulse. This final pulse is tailored to force the atoms to exit in whichever state is preferable for detection, in this case $|g\rangle$. If the phase of the atomic coherence at the overlap point matches the phase of the dark

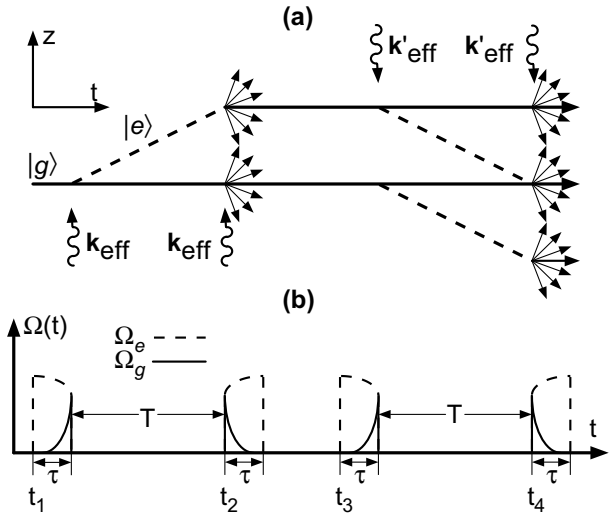

Fig. 9. Ramsey-Bordé interferometer based on adiabatic transfer. (a) Recoil diagram. At the second and fourth interactions, the multiple arrows indicate atoms that spontaneously emit because they are in the coupled state. For a three-level system, all of these atoms are optically pumped into $|g\rangle$, so they contribute to the background signal of the interferometer. In our actual experiment, we use circularly polarized light to induce transitions between the two $m_{\mathrm{F}} = 0$ Zeeman levels of the ground state. Atoms that undergo spontaneous emission tend to optically pump into the high angular momentum states. The diagram omits the spreading of the wave packets that occurs for nonzero τ. Neglecting ac Stark shifts, the interferometer phase shift depends only on T, not on τ. (b) The adiabatic passage pulse sequence required for implementing the interferometer shown in (a).

state, then the atom signal will be at a maximum. Scanning δ_{12} changes the relative phase of the atomic coherence and the field, allowing observation of fringes in the atom populations.

Creating an analog of the three pulse $\pi/2 - \pi - \pi/2$ interferometer using adiabatic transfer presents special difficulty due to the lack of a substitute for the π pulse. Similar problems limit the use of adiabatic transfer for creating large-area interferometers in which multiple stimulated Raman π pulses are used to further separate the arms of an interferometer. These limitations are discussed in an earlier work [42].

The atom interferometer geometry in Figure 8 modified to include a number of π-pulses sandwiched in between times t_2 and t_3 can be easily implemented using adiabatic transfer since for either the upper or lower interferometer, the atoms are in the same internal state when the π pulses

are applied. This is the approach presently used for the photon recoil measurement, which provides a factor of $N + 1$ enhancement of the sensitivity.

Another possible route for achieving large-area interferometers using adiabatic transfer is to apply a single adiabatic transfer pulse that involves the interchange of multiple photons, *e.g.*, using $\sigma^+ - \sigma^-$ beams to transfer an atom between the $m_{\rm F} = -F$ to $m_{\rm F} = +F$ ground state sublevels of an atom [35, 43]. For a valid dark state, the frequency width of the dark state must be larger than the total recoil splitting between the two states, which can require considerable laser powers for typical beam diameters. Also, these approaches generally involve the use of magnetic-field sensitive transitions. For most precision measurement experiments, magnetic-field inhomogeneities can not be controlled to the level that such transitions can be used.

A final consideration regarding the use of adiabatic transfer for atom interferometry is the level of background atoms that appear in the interferometer signal. In the present case of a collection of three-level systems, it would be difficult to distinguish the atoms transferred by adiabatic transfer from those transferred by optical pumping. On average, the momentum transfer would be smaller for optical pumping, but this would be hard to distinguish without sub recoil initial cooling of the atoms. Incorporating an adiabatic transfer pulse into an atom interferometer would reveal a loss of fringe contrast corresponding to the fraction of optically pumped atoms. In more complex systems, careful selection of beam polarizations allow optical pumping predominantly into states other than the states used for the adiabatic transfer. This allows the coherently and incoherently transferred atoms to be distinguished in the detection stage, so that the optical pumping does not cause a severe degradation of fringe contrast [39].

5.3 A measurement of the photon recoil and $\hbar/M$

In its simplest form, the photon recoil measurement records the Doppler shift of an atomic resonance caused by the momentum recoil from an absorbed photon. Consider the two-level atomic system of Figure 10a with two stable states $|a\rangle$ and $|b\rangle$. If the atom interacts with two counterpropagating, on-resonance fields, as in Figure 10b, then the difference $\omega_B - \omega_A$ contains a contribution from the momentum recoil of the photon absorbed in the first interaction. We use the differential measurement of Figure 10c. The first field puts the atom into a superposition of both momentum states. Two resonances exist for the second field frequency ω_B—one for each of the momentum states. The two pairs of momentum states coupled by ω_B have a velocity difference of $\Delta v = \frac{z\hbar k}{M_A}$, where $\hbar$ is the Planck constant, M_A is the atomic mass, and $k \sim k_A \sim k_B$ is the wave number of the light field. Ignoring the second- and higher-order Doppler shifts, which are insignificant for our experimental parameters, this velocity difference creates a Doppler-shift

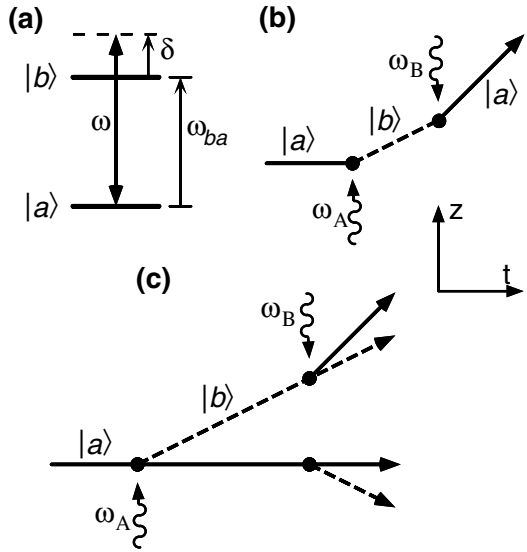

Fig. 10. Simplified version of the photon recoil measurement. The experiment is performed using the two-level atom in (a). The position of the atom relative to the initial unperturbed trajectory is shown as a function of time. The two field frequencies ω_A and ω_B are centered on resonance. (b) The difference $\omega_B - \omega_A$ includes a contribution from the momentum recoil caused by the absorption of a photon from the first interaction. (c) A simple modification converts this into a differential measurement which cancels out the contribution from the initial atomic velocity.

frequency difference between the two resonances of

$$\Delta f = \frac{k\Delta v}{2\pi} = \frac{2h\nu^2}{M_A c^2}, \tag{5.10}$$

where c is the speed of light and $\nu = ck/2\pi$ is the frequency of the light field.

The measurement can be further improved if we use a pair of $\pi/2$ pulses instead of single π pulses, ω_1 and ω_2 in much the same way that a Ramsey pulse pair is superior to a single Rabi pulse. Thus, we are naturally led to the Ramsey-Bordé interferometer shown in Figure 8a. The differential measurement is enhanced by maximizing the distance between the two interferometers as indicated schematically in Figure 8.

The fine structure constant α can be determined from the photon recoil measurement using the relation

$$\alpha^2 = \frac{2\mathrm{Ry}_\infty}{c}\frac{h}{m_\mathrm{e}}, \tag{5.11}$$

where Ry_∞ is the infinite-mass Rydberg constant and m_e is the electron mass. In our h/M_Cs experiment, we measure the frequency shift Δf for cesium atoms using light on resonance with the D_1 line. Assuming that ν is known accurately, equation (5.10) gives with high precision the ratio

$$\frac{h}{M_\mathrm{Cs}} = \frac{c^2\Delta f}{2\nu^2}\,. \tag{5.12}$$

Since Ry_∞ is known to 0.028 ppb [78] and c is defined, the uncertainty in the ratio of h/m_e limits the calculation of α from this relation. Expanding equation (5.11) using mass ratios, then substituting h/M_Cs from equation (5.12) gives

$$\alpha^2 = \frac{2\mathrm{Ry}_\infty}{c}\left(\frac{m_\mathrm{p}}{m_\mathrm{e}}\right)\left(\frac{M_\mathrm{Cs}}{m_\mathrm{p}}\right)\frac{h}{M_\mathrm{Cs}}. \tag{5.13}$$

The proton-electron mass ratio has been measured to 2.2 ppb [64]. The cesium-proton mass ratio is presently known only to 34 ppb [86], but may be improved in the near future to ~ 1 ppb [81]. We stabilize the laser frequency relative to the cesium D_1 line with an accuracy of about 0.3 ppb. The absolute frequency of this transition was known to 45 ppb [88] at the start of this measurement. However, this work prompted Udem, *et al.*, to measure the D_1 line to an accuracy of 12 parts in 10^{10} [76]. Consequently, an accurate measurement of Δf could determine α with an uncertainty below 1 ppb.

Presently the anomalous magnetic moment of the electron $a_\mathrm{e} \equiv (g-2)/2$ provides the most precise determination of the fine-structure constant α, with an uncertainty of 4.2 ppb (parts per billion). This approach equates the experimental value of a_e [87] with the quantum electrodynamics (QED) calculation of a_e as a power series in α [74] to determine a value for α. Consequently, the currently accepted value for α assumes the validity of QED. Improved precision in a QED-independent measurement of α thereby constitutes a test of QED. The goal of this work is a precision measurement of the recoil of an atom caused by the absorption of a photon. This result, when combined with an absolute frequency measurement and mass-ratio measurements, determines a value for α which does not require QED.

The most precise measurements of α, including this work at the time of Brent Young's thesis [55], with precision better than 100 ppb are shown in Figure 11. In addition to the a_e determination, these include measurements based on the quantum Hall effect [61], neutron diffraction [75], and

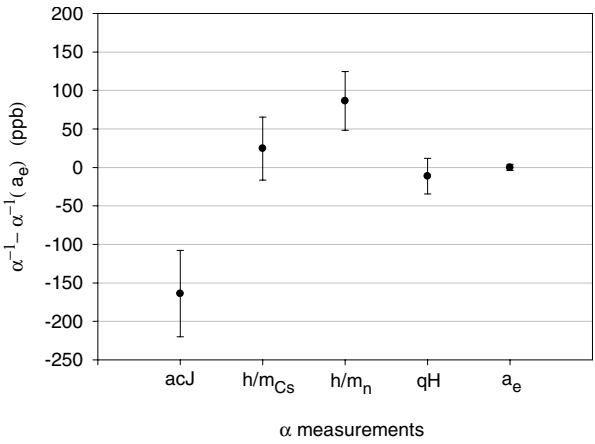

Fig. 11. Measurements of α better than 100 ppb. The values are plotted relative to $\alpha^{-1}(a_e) = 137.035\,999\,44(57)$ determined from the electron anomalous magnetic moment. These include results from the ac Josephson effect (acJ), this measurement (h/M_{Cs}), neutron diffraction (h/m_n), the quantum Hall effect (qH), and a_e.

the ac Josephson effect [92] with relative uncertainties of 24 ppb, 39 ppb, and 56 ppb, respectively. These measurements have statistically significant differences between them, and have considerably higher uncertainties than the a_e value, so another independent measurement of α would be of interest. Even the very precise a_e value recently changed 10σ because of a correction to the theory [74].

The neutron diffraction and photon recoil measurements, on the other hand, are independent of electrical definitions. The neutron diffraction and photon recoil measurements are conceptually very similar—the former measuring h/m_n and the latter h/m_{Cs}. Both approaches use quantum interference of neutral particles, so that they can easily be isolated from perturbing forces, and their interactions with matter are well understood. For neutron diffraction, the interferometer is generated by interactions of the neutrons with silicon crystals, the lattice spacing of which must be calibrated interferometrically. In the photon recoil measurement, the matter-wave interferometers are created by interactions with light fields propagating in vacuum. Accurate stabilization of the laser frequency provides an absolute calibration for the impulses created by the interferometer interactions. Reference [74] provides a comprehensive review of fine-structure constant measurements.

Many of the details of our h/M_{Cs} experiment have been described in the thesis of Brent Young [55]. The current level of precision in α is $\sim$4 ppb after 5 hours of integration time. At the present time, we are still searching

for systematic effects and hope to report a measurement with an absolute uncertainty in this range.

6 Atom gyroscopes

Consider an atom interferometer in an inertial (Galilean) frame of reference (x', y'). In this inertial frame, the atom goes in straight line trajectories. However, in a rotating laboratory frame, we see a distorted path. We use the Feynman formulation of quantum mechanics to calculate the phase-shift $\Psi(x_\mathrm{b}, t_\mathrm{b}) = \mathrm{e}^{S_\mathrm{Cl}/\hbar}\Psi(x_a, t_a)$ for the two paths Γ_I and Γ_II and follow the treatment given by Storey and Cohen-Tannoudji [16]. As before, S_Cl is the classical action, and in the inertial frame, it is given by

$$S_\mathrm{Cl} = \int_{\Gamma'} L'(\mathbf{x}', \dot{x}')\mathrm{d}t \tag{6.1}$$

$$= \int_{\Gamma'} \frac{1}{2} M \mathbf{v}'^2 \mathrm{d}t. \tag{6.2}$$

If we transform to the rotating (un-primed) frame a point a distance $\mathbf{r}$ from the axis of rotation will have velocity given by $\mathbf{v}' = \mathbf{v} + \Omega \times \mathbf{r}$. The Lagrangian in the rotating frame is

$$L(\mathbf{r}, \mathbf{v}) = L'(\mathbf{r}', \mathbf{v}') = \frac{1}{2} M \ [\mathbf{v} + (\mathbf{\Omega} \times \mathbf{r})]^2 \tag{6.3}$$

$$= \frac{1}{2} M \mathbf{v}^2 + M \mathbf{\Omega} \cdot (\mathbf{r} \times \mathbf{v}) + \frac{1}{2} M (\mathbf{\Omega} \times \mathbf{r})^2. \tag{6.4}$$

For an angular velocity Ω slow enough so that $\Omega \Delta t \ll 1$, where Δt is that transit time of the atoms through the interferometer, the rotation can be taken as a small perturbation.

$$L = L_0 + L_1 \tag{6.5}$$

$$= \frac{1}{2} M \mathbf{v}^2 + M \mathbf{\Omega} \cdot (\mathbf{r} \times \mathbf{v}) \tag{6.6}$$

where only the term to first order in Ω was kept. Thus, the phase difference between the two paths is then given by the action of the perturbing Lagrangian *integrated along the unperturbed (straight-line) paths*

$$\delta\phi = \frac{1}{\hbar} \int_{t_a}^{t_\mathrm{b}} L_1 \mathrm{d}t \tag{6.7}$$

$$= \frac{M\Omega}{\hbar} \int_{t_a}^{t_\mathrm{b}} [\mathbf{r}(t) \times \mathbf{v}(t)]\mathrm{d}t. \tag{6.8}$$

Using $\mathrm{d}\mathbf{r}/\mathrm{d}t = \mathbf{v}(t)$,

$$\delta\phi = \frac{M\Omega}{\hbar}\int_{t_a}^{t_\mathrm{b}} [\mathbf{r}(t) \times \mathrm{d}\mathbf{r}(t)] \tag{6.9}$$

$$= \frac{M\Omega}{\hbar}\int_{t_a}^{t_\mathrm{b}} 2\mathrm{d}(\mathrm{Area})\hat{\mathbf{z}} \tag{6.10}$$

$$= \frac{2M\Omega}{\hbar}A_0, \tag{6.11}$$

where A_0 is the total area of the triangle formed by the origin and the beginning and ending points $\mathbf{r}_a$ and $\mathbf{r}_\mathrm{b}$. Each interferometer path Γ_I and Γ_II consists of two straight-line segments. The phase difference between the two paths is given by

$$\Delta\phi = \Delta\phi|_{\Gamma_\mathrm{I}} - \Delta\phi|_{\Gamma_\mathrm{II}} \tag{6.12}$$

$$= \oint L_1(\mathbf{x}, \dot{\mathbf{x}})\mathrm{d}t \tag{6.13}$$

$$= \frac{2M\Omega}{\hbar}(\text{Enclosed area}). \tag{6.14}$$

This simple result could have been derived by considering a Mach-Zender interferometers in the shape of a circle. One calculates the difference in the number of oscillations of phase of the atom de Broglie wave going in circular clockwise and counter-clockwise directions. The atoms split by the first beamsplitter are rejoined after going halfway around the circle. However, if the apparatus is rotating during the transit time of the atoms, the second beamsplitter will have moved so as to introduce a path length difference. The phase difference is proportional to the area of the circle, the rotation rate and the mass of the atom. By considering infinitesimal changes in the shape of the paths, one can show that the formula applies to gyroscopes of arbitrary path shapes. The velocity and hence the de Broglie wavelength of the atom is not a factor: the shorter wavelength of faster moving atoms is counter-balanced by the shorter transit time of the atom through the apparatus.

6.1 A comparison of atom interferometers

Several matter wave gyroscopes have been constructed using cw optical beams [3,46], nanofabricated gratings [44,49], and micro fabricated shadow gratings [45, 50]. To date, the most sensitive instrument is the one constructed using off-resonant Raman pulses [46]. This interferometer uses a 2 meter long path with an enclosed area of 0.22 cm^2. Recent improvements such as the use of a transversely laser cooled atomic beam with a flux of 2×10^{10} atoms/s. Two beams, counterpropagating through the Mach-Zender path produce significant "common-mode" rejection by measuring

$|\Omega_{\mathrm{rot},+} - \Omega_{\mathrm{rot},-}| = |2\Omega_{\mathrm{rot},+}|$, where $\Omega_{\mathrm{rot},+}$ and $\Omega_{\mathrm{rot},-}$ are the rotations measured by the two opposing atomic beams. With these improvements, the sensitivity of the atom interferometer gyroscope was increased to 6×10^{-10} rad/s/$\sqrt{\mathrm{Hz}}$, or 8×10^{-6} of Earth's rotation per $\sqrt{\mathrm{Hz}}$ [47].

The relative performance of the various atom interferometers reflects a combination of inherent differences in the technologies and the experimental execution ("engineering") of the apparatus. Interferometers based on optical π and $\pi/2$ pulses have less stringent requirements on the velocity spread and divergence of the atom beam source as discussed in Section 3.1. It also may be intrinsically easier to compensate for vibrations since the optical phase of the light can be controlled with high bandwidth feedback systems and either acousto-optic, electro-optic or direct modulation of the laser frequencies. The error signal must still be referenced to a stable inertial platform. Atom interferometers based on material objects require mechanical isolation of all gratings and beamsplitters. Finally, Chu's Second Golden Rule states that a frequency or frequency-shift measurement is invariably superior to another measurement. However, interferometers as the one introduced by Kasevich and Chu [4], are phase measurements tied to the wavelength of light. A strictly *time-domain* measurement would be more accurate.

A comparison of atom interferometry measurements of gravity and rotations in listed in Table 2. The short term sensitivity of atom gyroscopes are now competitive with the best ring laser gyroscopes despite their short engineering time. There are no studies on the absolute accuracy and long term drift of atom interferometer gyroscopes. Work is now underway to study the long term stability of the instrument. So far, no work has been done trying to establish the absolute accuracy of these devices. Current drift rates produce a noise floor comparable to the short term stability. By contrast, the sensitivity of an atom interferometer gravimeter continues to improve out to integration times approaching 10^4 seconds.

Cryogenic gravimeters (a superconducting sphere levitated in a magnetic field) drift at the level of 2×10^{-10} g/day due to the changing mass of the sphere due to cryo-pumping. It is possible to calibrate these devices with an instrument that can measure an absolute value for g, but quantum flux jumps induced by vibrations prevent the device from being moved, once calibrated. Conventional spring/mass instruments, the current workhorse device used in oil and mineral exploration, have a drift of 3×10^{-8} g/day due to aging and thermal drift of the mechanical spring.

6.2 Future prospects

Atom interferometers are still in their infancy and one can expect significant improvements in sensitivity in the near future. Work has begun on atom interferometers based on multiple beam interference [52–54].

Table 2. Comparison of atom interferometer inertial sensors.

Rotation	**Short term sensitivity** rad/sec/$\sqrt{\text{Hz}}$
Raman Pulse [47]	6×10^{-10}
Moiré classical fringes [50]	2.25×10^{-9}
Nanofabricated gratings [49]	3.6×10^{-6}
Ring Laser gyro [48]	13×10^{-10}
Superfluid helium [44]	2×10^{-7}
Fiber optic gyro (commercial)	$\sim 3 \times 10^{-7}$

Acceleration due to gravity	**Short term sensitivity** g/$\sqrt{\text{Hz}}$	**Accuracy**
Raman pulse [31]	2×10^{-8}	5×10^{-9}
Moiré [50]	1.2×10^{-7}	not meas.
Spring/mass system	1×10^{-10}	not appl.
Cryogenic gravimeter	$< 10^{-12}$	not appl.
Falling corner cube	5×10^{-8}	2×10^{-9}

The basic idea is that optical resolution scales as the number of lines illuminated on a diffraction grating or as the effective number of bounces between the mirrors of a Fabry-Perot cavity. The hope is that multiple beam interference in atom interferometry will lead to a similar increase in resolution. Although these type of interferometers have yet to surpass the off-resonant Raman [31, 47], or adiabatic interferometers [55], excellent signals with as many as 160 interfering beams have been obtained [52].

Considerable attention is being paid to improving the atom beam source. However, it is worth remarking that the current state-of-the-art interferometers are not limited by the brightness of the source of atoms. For example, the short term sensitivity of the atomic fountain g-meter is *two orders of magnitude below the shot noise limit* imposed by the 3×10^6 atoms detected per launch cycle and four orders of magnitude below what is possible with high flux cold atom sources. Major noise sources in our instrument include high frequency phase noise (11 ppb), background fluctuations (7 ppb), residual vibration and rotation noise (5 ppb), Raman laser intensity noise (3.5 ppb), and the frequency stability of the Loran-C receiver (3.0 ppb).

There are several groups working to develop atom interferometers based on Bose-condensed atoms. The reasons for this push include (1) the higher

brightness of a Bose condensate would mean less transverse spreading during long atomic fountain times (2) the spatial distribution of the cloud of atoms would be better characterized (useful for understanding potential systematic effects), and (3) the well-defined momentum distribution would allow well-separated transitions between the same internal state but different momentum states (*e.g.* $|g, \mathbf{p}\rangle \leftrightarrow |g, \mathbf{p} + 2\hbar\mathbf{k}_{\rm eff}\rangle$) [56].

There are also a number of groups working towards the demonstration of atom waveguides suitable for atom interferometers.

Acknowledgements

This work was supported in part from grants by the NSF, AFOSR. The author also wishes to thank K.Y. Chung for assistance in the preparation of the figures for this manuscript.

References

[1] O. Carnal and J. Mlynek, *Phys. Rev. Lett.* **66** (1991) 2689.

[2] D.W. Keith, C.R. Ekstrom, Q.A. Turchette and D.E. Pritchard, *Phys. Rev. Lett.* **66** (1991) 2693.

[3] F. Riehle, Th. Kisters, A. Witte, J. Helmcke and Ch. Borde, *Phys. Rev. Lett.* **67** (1991) 177.

[4] M. Kasevich and S.Chu, *Phys. Rev. Lett.* **67** (1991) 181-184.

[5] C.S. Adams, *Contemp. Phys.* **35** (1994) 1-19.

[6] N.F. Ramsey, *Molecular Beams* (Oxford University Press, Oxford, 1956).

[7] L. Allen and J.H. Eberly, *Optical Resonances and Two-Level Atoms* (Dover, New York, 1975).

[8] B. Young, M. Kasevich and S. Chu, in *Atom Interferometry*, edited by P. Berman (Academic Press, San Diego, 1997) pp. 363-406.

[9] C. Cohen-Tannoudji, B. Diu and F. Laloë, *Quantum Mechanics* (Wiley, New York, 1977).

[10] R.P. Feynman and A.R. Hibbs, *Quantum Mechanics and Path Integrals* (McGraw-Hill, New York, 1965).

[11] We follow the presentation in C.S. Adams, O. Carnal and J. Mlynek, in *Advances in Atomic, Molecular and Optical Physics* **34**, pp. 1-33.

[12] The Feynman approach was used by M. Kasevich and S. Chu, *Phys. Rev. Lett.* **67** (1991) 181, in their calculation of the phase of an atom interferometer based on optical pulses where the different internal energy of the atomic states were considered. This treatment follows the tutorial by Storey and Cohen-Tannoudji [16].

[13] J. Ishikawa, F. Riehle, J. Helmcke and Ch. Bordé, *Phys. Rev. A* **49** (1994) 4794.

[14] R. Friedberg and S.R. Hartman, *Phys. Rev. A* **48** (1993) 1446.

[15] D.S. Weiss, B.C. Young and S. Chu, *Appl. Phys. B* **59** (1994) 217.

[16] P. Storey and C. Cohen-Tannoudji, *J. Phys. II France* **4** (1994) 1999.

[17] M. Kasevich and S. Chu, *Appl. Phys. B* **54** (1992) 321.

[18] Y.V. Baklanov, B.Y. Dubetsky and V.P. Chebotayev, *Appl. Phys.* **38** (1997) 159.

[19] J.C. Bergquist, S.A. Lee and J.L. Hall, *Phys. Rev. Lett.* **38** (1997) 159.

[20] Ch. J. Bordé, C. Salomon, S. Avrillier, A. Van Lerberghe, C. Bréant, D. Bassi and G. Scoles, *Phys. Rev. A* **30** (1984) 1836.

[21] D.S. Weiss, B.C. Young and S. Chu, *Phys. Rev. Lett.* **70** (1993) 2706.

[22] See J. Schmiedmayer *et al.*, in *Atom Interferometry*, edited by P. Berman (Academic Press, San Diego, 1997) pp. 1-83, and references contained within.

[23] J.F. Clauser and S. Li, in *Atom Interferometry*, edited by P. Berman (Academic Press, San Diego, 1997) pp. 121-152.

[24] B. Dubetsky and P.R. Berman, in *Atom Interferometry*, edited by P. Berman (Academic Press, San Diego, 1997) pp. 407-468.

[25] V.P. Chebotayev, B. Dubetsky, A.P. Kazantsev and V.P. Yakovlev, *J. Opt. Soc. Am. B* **2** (1985) 1791.

[26] M.S. Chapman, C.R. Ekstrom, T.D. Hammond, J. Schmiedmayer, B.E. Tannian, S. Wehinger and D.E. Pritchard, *Phys. Rev. A* **51** (1995) R14.

[27] J.F. Clauser and S. Li, *Phys. Rev. A* **49** (1994) R2213.

[28] P.L. Gould, G.A. Ruff and D.E. Pritchard, *Phys. Rev. Lett.* **56** (1986) 827.

[29] D.M. Greenberger and A.W. Overhauser, *Rev. Mod. Phys.* **51** (1979) 43.

[30] J. Hensley, A. Peters and S. Chu, *Rev. Sci. Instrum.* **XXXX** (1997).

[31] A.Peters, K.Y. Chung and S. Chu, *Nat* **400** (1999) 849.

[32] U. Gaubatz, P. Rudecki, M. Becker, S. Schiemann, M. Külz and K. Bergmann, *Chem. Phys. Lett.* **149** (1988) 463.

[33] C.J. Bordé, C. Salomon, S. Avrillier, A. Van Lerberghe, C. Bréant, D. Bassi and G. Scoles, *Phys. Rev. A* **30** (1984) 1836.

[34] P. Marte, P. Zoller and J.L. Hall, *Phys. Rev. A* **44** (1991) R4118.

[35] L.S. Goldner, C. Gerz, R.J.C. Spreeuw, S.L. Rolston, C.I. Westbrook, W.D. Phillips, P. Marte and P. Zoller, *Phys. Rev. Lett.* **72** (1994) 997.

[36] P. Pillet, C. Valentin, R.-L. Yuan and J. Yu, *Phys. Rev. A* **48** (1993) 845.

[37] J. Lawall and M. Prentiss, *Phys. Rev. Lett.* **72** (1994) 993.

[38] J. Oreg, F.T. Hioe and J.H. Eberly, *Phys. Rev. A* **29** (1984) 690.

[39] M. Weitz, B.C. Young and S. Chu, *Phys. Rev. Lett.* **73** (1994) 2563.

[40] M. Weitz, B.C. Young and S. Chu, *Phys. Rev. A* **50** (1994) 2438.

[41] J.R. Kuklinski, U. Gaubatz, F.T. Hioe and K. Bergmann, *Phys. Rev. A* **40** (1989) 6741.

[42] B. Young, M. Kasevich and S. Chu, in *Atom Interferometry*, edited by P. Berman (Academic Press, 1997) pp 363-406.

[43] P.D. Featonby, G.S. Summy, J.L. Martin, H. Wu, K.P. Zetie, C.J. Foot and K. Burnett, *Phys. Rev. A* **53** (1996) 373.

[44] J. Schmiedmayer *et al.*, in *Atom Interferometry*, edited by P. Berman (Academic Press, 1997) pp. 1-84.

[45] H. Batelaan *et al.*, in *Atom Interferometry*, edited by P. Berman (Academic Press, 1997) pp. 85-120.

[46] T.L. Gastavson, P. Boyer and M.A. Kasevich, *Phys. Rev. Lett.* **78** (1997) 2046.

[47] T.L. Gastavson, Ph.D. Thesis (2000).

[48] C.H. Rowe *et al. Appl. Opt.* **38** (1999) 2516.

[49] A. Lenef *et. al.*, *Phys. Rev. Lett.* **78** (1997) 760.

[50] M.K. Oberthaler *et al.*, *Phys. Rev. A* **54** (1997) 3165.

[51] See also the discussion in K. Sengstock, U. Sterr, G. Hennig, D. Bettermann, J.H. Müller and W. Ertmer, *Opt. Commun.* **103** (1993) 73.

[52] H. Hinderthür *et al.*, *Phys. Rev. A* **59** (1999) 2216.

[53] H. Hinderthür *et al.*, *Phys. Rev. A* **56** (1997) 2085.
[54] M. Weitz, T. Heupel and T.W. Hänsch, *Phys. Rev. Lett.* **77** (1996) 2356.
[55] Brent Young, Ph.D. Thesis (1997).
[56] M. Kozuma *et al.*, *Phys. Rev. Lett.* **82** (1999) 871.
[57] Y.V. Baklanov, B.Y. Dubetsky and V.P. Chebotayev, *Appl. Phys.* **9** (1976) 171.
[58] J.C. Bergquist, S.A. Lee and J.L. Hall, *Phys. Rev. Lett.* **38** (1977) 159–162.
[59] C.J. Bordé, C. Salomon, S. Avrillier, A. Van Lerberghe, C. Bréant, D. Bassi and G. Scoles, *Phys. Rev. A* **30** (1984) 1836–1848.
[60] C.J. Bordé, In Laser Spectroscopy X, edited by M. Duclos, E. Giacobino, and G. Camy, World Scientific, Singapore (1992) pp. 239–245
[61] M.E. Cage, R.F. Dziuba, R.E. Elmquist, B.F. Field *et al.*, *IEEE Trans. Instrum. Meas.* **38** (1989) 284–289.
[62] S. Chu, L. Hollberg, J.E. Bjorkholm, A. Cable and A. Ashkin, *Phys. Rev. Lett.* **55** (1985) 48–51.
[63] C. Cohen-Tannoudji, B. Diu and F. Laloë, Quantum Mechanics (John Wiley & Sons, New York, 1977).
[64] D.L. Farnham, R.S. Van Dyck Jr and P.B. Schwinberg, *Phys. Rev. Lett.* **75** (1995) 3598–3601.
[65] R. Friedberg and S.R. Hartmann, *Phys. Rev. A* **48** (1993) 1446–1472.
[66] U. Gaubatz, P. Rudecki, M. Becker, S. Schiemann, M. Külz and K. Bergmann, *Chem. Phys. Lett.* **149** (1988) 463–468.
[67] U. Gaubatz, P. Rudecki, S. Schiemann and K. Bergmann, *J. Chem. Phys.* **92** (1990) 5363–5376.
[68] G. Grynberg, J. DuPont-Roc, S. Haroche and C. Cohen-Tannoudji, *J. Phys. (Paris)* **34** (1973) 537–558.
[69] J.M. Hensley, A. Peters and S. Chu (1996) (private communication).
[70] J. Ishikawa, F. Riehle, J. Helmcke and C.J. Bordé, *Phys. Rev. A* **49** (1994) 4794–4825.
[71] M. Kasevich and S. Chu, *Phys. Rev. Lett.* **67** (1991) 181–184.
[72] M. Kasevich and S. Chu, *Appl. Phys. B* **54** (1992) 321–332.
[73] T. Kinoshita, *IEEE Trans. Instrum. Meas.* **44** (1995) 498–500.
[74] T. Kinoshita, *Rep. Prog. Phys.* **59** (1996) 1459–1492.
[75] E. Kruger, W. Nistler and W. Weirauch, *IEEE Trans. Instrum. Meas.* **44** (1995) 514.
[76] Th. Udem, J. Reichert, R. Holzwarth and T.W. Hänsch, *Phys. Rev. Lett* **82** (1999) 3568–3571.
[77] P. Marte, P. Zoller, and J.L. Hall, *Phys. Rev. A* **44** (1991) R4118–R4121.
[78] F. Nez, M.D. Plimmer, S. Bourzeix *et al.*, *Phys. Rev. Lett.* **69** (1992) 2326–2329.
[79] G. Peter, F.J. Klopping, G.S. Sasagawa, J.E. Faller and T.M. Niebauer, *J. Geophys. Res.* **98** (1993) 4619–4626.
[80] A. Peters, K. Chung and S. Chu (1996) (private communication).
[81] D.E. Pritchard (1996) (private communication).
[82] N.F. Ramsey, *Phys. Rev.* **78** (1950) 695–699.
[83] N.F. Ramsey, *Mol. Beams* (Oxford University Press, Oxford, 1956).
[84] J.J. Sakurai, *Modern Quant. Mech.* (Addison-Wesley, Reading, 1994).
[85] C.P. Slichter, *Principles of Magnetic Resonance*, 3rd Ed. (Springer-Verlag, 1990).
[86] H. Stolzenberg, S. Becker, G. Bollen *et al.*, *Phys. Rev. Lett.* **65** (1990) 3104–3107.
[87] R.S. Van Dyck Jr, P.B. Schwinberg and H.G. Dehmelt, *Phys. Rev. Lett.* **59** (1987) 26.

[88] K.-H. Weber and C.J. Sansonetti, *Phys. Rev. A* **35** (1987) 4650–4660.

[89] D.S. Weiss, B.C. Young and S. Chu, *Phys. Rev. Lett.* **70** (1993) 2706.

[90] D.S. Weiss, B.C. Young and S. Chu, *Appl. Phys. B* **59** (1994) 217–256.

[91] S.A. Werner, J.-L. Staudenmann and R. Colella, *Phys. Rev. Lett.* **42** (1979) 1103–1006.

[92] E.R. Williams, G.R. Jones Jr, S. Ye, R. Liu, H. Sasaki, P.T. Olsen, W.D. Phillips and H.P. Layer, *IEEE Trans. Instrum. Meas.* **38** (1989) 233–237.